



Πρόγραμμα Μεταπτυχιακών Σπουδών
στη Φυσική
Τμήμα Φυσικής
Σχολή Θετικών Επιστημών
Πανεπιστήμιο Ιωαννίνων

ΜΕΤΑΠΤΥΧΙΑΚΗ ΔΙΠΛΩΜΑΤΙΚΗ ΕΡΓΑΣΙΑ (Μ.Δ.Ε.)

Εφαρμογή σχημάτων σύμφωνου
ελέγχου $\omega/2\omega$ στη μικροσκοπία
φωτοϊονισμού των μη-υδρογονικών
ατόμων

ΕΛΕΥΘΕΡΙΑ ΤΖΑΛΛΑ
Αριθμός μητρώου: 829

Επιβλέπων καθηγητής: Σαμουήλ Κοέν

Ιωάννινα
Φεβρουάριος 2025



Postgraduate Studies in Physics
Department of Physics
School of Sciences
University of Ioannina

MASTER THESIS

**Application of $\omega/2\omega$ phase-sensitive
coherent-control excitation schemes to
photoionization microscopy of
non-hydrogenic atoms**

ELEFThERIA TZALLA
ID Number: 829

Supervisor: Samuel Cohen

Ioannina
February 2025

Abstract

The term “photoionization microscopy” (PM) refers to an experimental technique that images the outgoing flux of slow (meV) electrons produced during atomic photoionization in the presence of a homogeneous static electric field. The energy region of interest lies near the ionization threshold, where continuum Stark states coexist with quasibound ones (resonances). The main purpose of PM is to record and unveil the features of resonances. Particularly for the quasibound states of the hydrogen atom, the excited electron is ionized solely via tunneling, in contrast to the continuum states, where the electron escapes freely. However, in non-hydrogenic atoms, resonances and continua are coupled, making the recording of the former more challenging. To overcome these difficulties, we theoretically examine a scheme of simultaneous one- and two-photon excitation of the final Stark states using two coherent laser beams with frequencies 2ω and ω , respectively, and an experimentally controlled phase difference $\Delta\Phi$ between them. Specifically, by applying the Harmin-Fano Stark theory, the aforementioned technique is modeled for the sodium (Na) atom and by adopting as initial states either the 3s ground state or the 3p first excited one. The necessary input Na data for the model (energy levels, one and two photon matrix elements) is computed using a parametric potential that is available in the literature. The results of our study show that, indeed, with an optimal selection of the energy range, the intensities and the phase difference $\Delta\Phi$ of the light beams, the calculated images (current probability density) reveal the resonant characteristics, while those corresponding to exclusive one- or two-photon transitions simply display only the features of the degenerate continua. Finally, the form of the images is also studied in the vicinity of avoided crossings between interacting quasibound states.

Περίληψη

Ο όρος «μικροσκοπία φωτοϊονισμού» (ΜΦ) αναφέρεται στην πειραματική απεικονιστική τεχνική καταγραφής της εξερχόμενης ροής των αργών (meV) ηλεκτρονίων που παράγονται κατά τον φωτοϊονισμό των ατόμων υπό την παρουσία ομογενούς στατικού ηλεκτρικού πεδίου. Η ενεργειακή περιοχή ενδιαφέροντος της τεχνικής είναι κοντά στο κατώφλι ιονισμού, όπου συνυπάρχουν καταστάσεις Stark του συνεχούς και ημιδέσμιες (συντονισμοί). Κύριος σκοπός της ΜΦ είναι να καταγράψει και να αναδείξει τα χαρακτηριστικά των συντονισμών. Σε αυτές τις ημιδέσμιες καταστάσεις, και ειδικά για το άτομο του υδρογόνου, το διεγερμένο ηλεκτρόνιο ιονίζεται αποκλειστικά μέσω του φαινομένου σήραγγας, σε αντίθεση με το συνεχές όπου το ηλεκτρόνιο διαφεύγει ανεμπόδιστα. Ωστόσο, στα μη-υδρογονικά άτομα, οι συντονισμοί είναι συζευγμένοι με τα συνεχή και η καταγραφή τους είναι δυσκολότερη. Για να ξεπεραστούν αυτές οι δυσκολίες, στη παρούσα εργασία εξετάζεται θεωρητικά ένα σχήμα ταυτόχρονης μονοφωτονικής και διφωτονικής διέγερσης των τελικών καταστάσεων Stark από δύο σύμφωνες φωτεινές δέσμες laser με συχνότητες 2ω και ω , αντίστοιχα, και πειραματικά ελεγχόμενη μεταξύ τους διαφορά φάσης $\Delta\Phi$. Συγκεκριμένα, χρησιμοποιώντας τη θεωρία Stark των Harmin και Fano, η παραπάνω τεχνική μοντελοποιείται στο άτομο του νατρίου (Na) για διέγερση από δύο αρχικές καταστάσεις, τη θεμελιώδη $3s$ και την πρώτη διεγερμένη $3p$. Τα απαραίτητα στοιχεία εισόδου στο μοντέλο που αφορούν στο Na (ενεργειακά επίπεδα, μονοφωτονικά και διφωτονικά στοιχεία πίνακα), υπολογίζονται με τη χρήση ενός διαθέσιμου στη βιβλιογραφία παραμετρικού δυναμικού. Τα αποτελέσματα της μελέτης δείχνουν ότι, πράγματι, με κατάλληλη επιλογή της ενεργειακής περιοχής, των εντάσεων των φωτεινών δεσμών και της $\Delta\Phi$ οι καταγραφόμενες εικόνες (ρεύμα πυκνότητας πιθανότητας) εμφανίζουν τον χαρακτήρα των συντονισμών, ενώ αυτές που αντιστοιχούν σε αποκλειστική μονοφωτονική ή διφωτονική μετάβαση εμφανίζουν μόνον τον χαρακτήρα των ενεργειακά εκφυλισμένων συνεχών. Τέλος, στη εργασία διερευνήθηκαν οι καταγραφόμενες εικόνες στη γειτονιά αλληλεπιδρόντων ημιδέσμιων καταστάσεων.

Table of Contents

1	Introduction	1
2	Theory	4
2.1	Hydrogenic Stark Effect and Photoionization Microscopy	4
2.2	Multielectron atoms	8
2.3	Matrix Elements in a bichromatic field	9
2.4	Excitation schemes	11
2.5	Contrast and Optimization	16
3	Results and Discussion	18
3.1	PSCC just above the saddle point energy	18
3.1.1	$m = 0$ final Stark states	18
3.1.2	$ m = 1$ final Stark states	23
3.2	PSCC with many continuum channels	33
	Conclusions	37
A	Alkali atoms: Energy levels and Wave functions	39

1 | Introduction

Our comprehension of systems at the atomic scale leans on quantum mechanics and the concept of the wave function, which provides insight into predicting a system's properties. However, until recently the wave function itself was not measured directly in an experiment, but the information about it was inferred through the comparison of experimentally obtained observables, such as absorption or emission spectra, with the corresponding theoretical predictions.

Over the years, significant advancements have been made in developing experimental techniques aimed at determining the wave function itself. One prominent example is photoionization microscopy (PM), which involves the near-threshold ionization of atoms under the presence of a static electric field. These experiments utilize charged-particle imaging spectrometers, such as the velocity map imaging (VMI) ones, which mainly consist of a laser-atom interaction region—where the electric field is applied—and a two-dimensional position sensitive detector (PSD) placed perpendicular to the field axis. These spectrometers capture the electron current probability density resulting from photoionization and whose study enables (when the energy of the produced electrons is sufficiently low, i.e., in the meV range) the visualization of quantum interference patterns in the recorded images. It turns out that these interference phenomena reflect the squared modulus of the projection of the electron's wave function to the detector's plane. The term “microscopy” is particularly fitting in this context, as the outgoing photoelectron wave function extends over macroscopically large distances along the direction of the field, while remaining confined transversely to it.

PM was first theoretically proposed in the 1980s, and thoroughly analyzed by Kondratovitch and Ostrovsky [1–4] within the framework of the hydrogenic Stark effect theory, which utilized semi-classical descriptions based on parabolic wave functions [5, 6]. It was shown that the presence of the external electric field lowers the ionization limit and allows for the near-threshold coexistence of continua, where the electron can escape freely, and quasi-bound Stark states, also called resonances, where the electron is initially bound but can escape via tunneling. Although PM has the potential to provide insights into the wave functions of both types of states, the primary focus was on imaging the wave functions associated with resonant states. While the measurement of continuum wave functions have been successfully realised

in studies dealing with photodetachment [7], the accurate measurement of resonant features remains a relatively recent and significant accomplishment.

Early PM experiments were conducted on xenon (atomic number $Z = 54$), a non-hydrogenic atom with a large ionic core [8–10]. In such multi-electron systems, short-range interactions arise due to the interaction between the excited electron and the residual ionic core. These interactions result in Stark states that are expressed as mixtures of hydrogenic quasi-bound and continuum parabolic states. This mixing causes a significant portion of the initial resonant state population to spread across multiple degenerate continua, leading to comparable excitation amplitudes of both resonant and continuum states. This strong resonance-continuum coupling, driven by the ionic core size, significantly weakens the visibility of the resonant structures, making them challenging to record.

The findings from xenon experiments highlighted that for resolving resonant features it is necessary to minimize the coupling between the resonances and continua (which depends on the ion's size and atomic number Z), as well as to reduce the number of continua present and, if possible, diminish their excitation. To address these challenges, the most straightforward approach was to shift towards lighter atoms, which led to PM studies on lithium (Li, $Z = 3$) [11, 12], helium (He, $Z = 2$) [13], along with those on the hydrogen (H) atom itself [14], where the simpler atomic structure and the absence of coupling between resonances and continua allowed for a clearer observation of resonant features.

The results of the hydrogen experiments [14] not only validated theoretical predictions [1–4, 15–17] but were also recognized as one of the most significant discoveries in Physics in 2013. In Li, resonant features were clearly detected, albeit noticeably weaker than those observed in the H experiments. In contrast, He experiments demonstrated resonant characteristics nearly as prominent as those in H. This was attributed to measurements conducted near avoided crossings between pairs of interacting resonances [18], with the resonance of interest being effectively decoupled from the continua. Finally more recent experiments extended this research to the medium-sized magnesium atom (Mg, $Z=12$), where several resonant manifestations were recorded. However, these features were relatively weak compared to those seen in lighter atoms [19].

In parallel with experimental progress, a series of theoretical studies proposed that resonances in multi-electron systems could be effectively depicted under specific conditions (spatial and spectral resolution, optimal choice of field strength etc.) [20–22]. For example, other investigations of non-hydrogenic atoms—particularly Alkali metal atoms such as sodium (Na)—showed that the prominence of resonances in PM images depends heavily on the field strength, which should be carefully chosen [23]. All these studies emphasized that focusing on energy regions just above the ionization threshold—where the number of continua remains low—could substantially enhance the resonant characteristics in PM images [11, 12].

Moreover, earlier as well as recent theoretical PM studies for the hydrogen atom

demonstrated the weakening of the excitation of the continua, via the interference between two excitation amplitudes describing the population transfer from an initial state to the final Stark states. These amplitudes are induced by the interaction of a bichromatic laser field composed of a fundamental frequency laser beam and one of its mutually coherent harmonics. Each beam corresponds to a distinct excitation pathway, coupling the same initial and final states but through different photon absorption processes. As a result, quantum interference occurs between these two pathways. By externally adjusting the relative phase between the two fields, phase-sensitive coherent-control (PSCC) can be achieved [24, 25]. Carefully selecting the intensities of the two beams and tuning the relative phase allows the manipulations of the targeted observables. The method of two-pathway quantum interference, along with PSCC, has been successfully used in the past to manipulate population transfer between two bound states [26], as well as control of energy and angular distributions of photoionization products [27].

Building on previous theoretical proposals and experimental findings, in this work we examine a PSCC scheme that utilizes two coherent laser fields with frequencies $\omega_1 = \omega$ and $\omega_2 = 2\omega$, along with an experimentally controlled phase difference $\Delta\Phi$ between them. In contrast, however, with the earlier study which was devoted to hydrogen atom, here we focus on the more realistic and significant problem of non-hydrogenic atoms. To this end we employ the Fano-Harmin Frame Transformation Theory (FTT) for the Stark effect, as it may be applied to the Alkali atoms. The choice of ω , 2ω bichromatic laser field was motivated by its straightforward implementation in an setup.

Our calculations are mainly focused on the energy range near the Stark-downshifted ionization threshold, where the number of continua is limited. Our results for the atom of sodium (Na) demonstrate that by carefully selecting the laser intensities and $\Delta\Phi$, excitation to the continuum can be indeed minimized, enabling nearly exclusive excitation of resonances. Additionally, motivated by the He study [13], the present work focused in energy ranges near avoided crossings between interacting quasi-bound states.

The necessary input data for the aforementioned Na atom (energy levels, one- and two-photon transition matrix elements) were computed using a spherically symmetric parametric model potential, that depends on the angular momentum quantum number ℓ of the valence electron. This required parametric potential was obtained from the literature [28], with certain adjustments made to ensure the desired stability and level of precision.

We believe that the perspectives opened by this study enable the extension of PM to more complex quantum systems, broadening the scope of applications in atomic and molecular physics.

2 | Theory

2.1 Hydrogenic Stark Effect and Photoionization Microscopy

The principles of photoionization microscopy (PM) are rooted in the quantum description of the hydrogen atom under the influence of a static electric field, a phenomenon known as the hydrogenic Stark effect [15]. In hydrogen, the interaction of the electron with the external field augments the spherically symmetric Coulomb attraction of the nucleus. As a result, the total interaction lacks spherical symmetry, causing the orbital angular momentum of the electron to cease being a constant of motion. However, the projection of the angular momentum along the direction of the field remains conserved.

The quantum mechanical framework for describing this system is based on the solution of the relevant time-independent Schrödinger equation. For the hydrogen atom in the presence of a homogeneous static electric field $\mathbf{F} = F\mathbf{z}$, and neglecting spin-orbit effects, the Coulomb-Stark potential is expressed in atomic units (a.u., $e = m_e = \hbar = (4\pi\epsilon_0)^{-1} = 1$)—which are used throughout this study unless stated otherwise—as,

$$U_{cs}(\mathbf{r}) = -\frac{Z}{r} + Fz \quad (2.1)$$

with $r = [x^2 + y^2 + z^2]^{1/2}$ the radial spherical coordinate, and Z the nuclear charge, $Z = 1$ for the hydrogen atom. The U_{cs} is depicted in Figure 2.1(a), in which it can be observed that the static electric field “opens” the Coulomb trap towards the negative z region. A cut of the two dimensional potential surface along the z -axis is presented in Figure 2.1(b), in which two characteristic energies are highlighted.

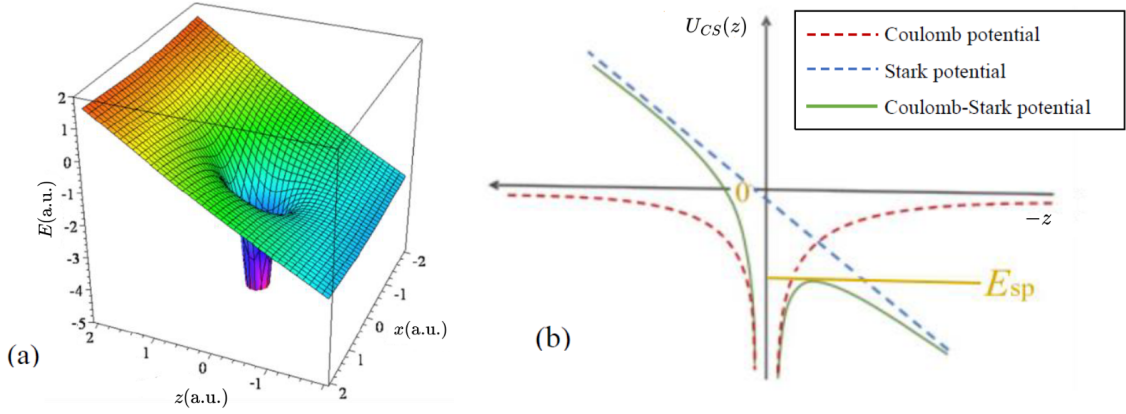


Figure 2.1: (a) Coulomb-Stark potential for the hydrogen atom. (b) Two dimensional potential $U_{CS}(z)$ along the z -axis, E_{sp} is represented by the horizontal yellow line.

The first is the zero-field ionization threshold, corresponding to $E = 0$ in the absence of the static field ($F = 0$), and the second is the field induced ionization limit, defined by the saddle point energy E_{sp} , which is given by,

$$E_{sp} = -2\sqrt{ZF}. \quad (2.2)$$

In this study, we are interested in the energy range near E_{sp} , that is $-|E_{sp}| < E < 0$. Additionally, it would be convenient for the following discussion to introduce the reduced energy variable

$$\varepsilon \equiv E/|E_{sp}|. \quad (2.3)$$

The aforementioned Schrödinger equation, incorporating the Coulomb-Stark potential of Eq.(2.1) takes the form:

$$\left[-\frac{1}{2}\nabla^2 - \frac{Z}{r} + Fz - E \right] \psi(\mathbf{r}) = 0 \quad (2.4)$$

with E the energy of the system. Notably, the above equation is separable in semi-parabolic coordinates [29]

$$\chi = [r + z]^{1/2} \geq 0, \quad v = [r - z]^{1/2} \geq 0, \quad \varphi = \tan^{-1}(y/x) \quad (2.5)$$

allowing the wave function to be expressed in the form

$$\psi(\mathbf{r}) = [2\pi\chi v]^{-1/2} X(\chi)Y(v)e^{im\varphi} \quad (2.6)$$

where $m = 0, \pm 1, \pm 2, \dots$ is the magnetic quantum number with respect to the static field axis [29]. Substituting $\psi(\mathbf{r})$ into the Schrödinger equation, we obtain two

2.1. Hydrogenic Stark Effect and Photoionization Microscopy Chapter 2. Theory

decoupled differential equations for the wave functions X and Y , which are written as follows [30, 31],

$$\left[-\frac{1}{2} \frac{d^2}{d\chi^2} + U_{X,eff}(\chi) - 2Z_1 \right] X(\chi) = 0, \quad U_{X,eff}(\chi) = \frac{4m^2 - 1}{8\chi^2} + \frac{F\chi^4}{2} - E\chi^2 \quad (2.7)$$

$$\left[-\frac{1}{2} \frac{d^2}{dv^2} + U_{Y,eff}(v) - 2Z_2 \right] Y(v) = 0, \quad U_{Y,eff}(v) = \frac{4m^2 - 1}{8v^2} - \frac{Fv^4}{2} - Ev^2. \quad (2.8)$$

These equations include the separation constants Z_1 and Z_2 , which are related by $Z_1 + Z_2 = Z$ and act as eigenvalues to the respective differential equations. The electron's motion in the χ coordinate is bound, whereas ionization occurs only along the v coordinate. Therefore, this constitutes a scattering problem that can be solved for specified values of m , F , and energy E .

The bound nature of the electron's motion along the χ coordinate imposes the asymptotic condition $X(\chi \rightarrow \infty) \rightarrow 0$, leading to the quantization of Z_1 . This results in a set of values of $Z_1^{n_1,|m|}$, with $n_1 = 0, 1, 2, \dots$ being the number of nodes of the wave function $X_{n_1,|m|}(\chi)$. Each given eigenvalue $Z_1^{n_1,|m|}$ also determines the corresponding value of $Z_2^{n_1,|m|} = Z - Z_1^{n_1,|m|}$. On the other hand, at small values of χ ($\chi \rightarrow 0$), the wave function satisfies the condition $X(\chi \rightarrow 0) = 0$.

For the v coordinate, the behavior is analogous for small values ($v \rightarrow 0$), where $Y(v \rightarrow 0) = 0$. However, as $v \rightarrow \infty$ the wave function $Y(v)$ transitions to a WKB (Wentzel-Kramers-Brillouin) form [32],

$$Y(v \rightarrow \infty) = \frac{C_Y}{k^{1/2}(v)} \sin[\theta(v) + \phi_0] \quad (2.9)$$

signaling electron ionization. In Eq.(2.9), $k^2(v) = 2[2Z_2^{n_1,|m|} - U_{Y,eff}(v)]$ is the electron's wavenumber function and the function $\theta(v)$ is given by,

$$\theta(v) = \int^v k(v') dv'. \quad (2.10)$$

The experimentally recorded quantity of interest is the outgoing flux of ionized electrons out of an initial state ψ_i , given by the probability current density,

$$\mathbf{J} = -\frac{1}{2i} [\psi_{out}^+ \nabla(\psi_{out}^+)^* - (\psi_{out}^+)^* \nabla(\psi_{out}^+)]. \quad (2.11)$$

As previously mentioned, the electron can escape to infinity solely via the v -coordinate, so we are interested in the projection,

$$J_v \Big|_{v=v_{det}} = \mathbf{J} \cdot \hat{e}_v = -\frac{1}{2i} \frac{1}{\sqrt{\chi^2 + v^2}} \left[\psi_{out}^+ \frac{\partial(\psi_{out}^+)^*}{\partial v} - (\psi_{out}^+)^* \frac{\partial\psi_{out}^+}{\partial v} \right] \Big|_{v=v_{det}} \quad (2.12)$$

2.1. Hydrogenic Stark Effect and Photoionization Microscopy Chapter 2. Theory

along a paraboloid defined by constant $v = v_{det}$ [17]. For sufficiently large v_{det} , and within the relevant range of electron impact radius values $\rho = \chi v_{det}$, this paraboloid approximates the plane of the PSD. The latter is oriented perpendicularly to the z -axis and positioned at $z_{det} = -v_{det}^2/2$.

The outgoing wave function ψ_{out}^+ can be determined by solving the time-dependent Schrödinger equation using first-order perturbation theory. This leads to the so-called ‘‘Schrödinger equation with a source’’ [15],

$$\left[-\frac{1}{2}\nabla^2 - \frac{Z}{r} + Fz - E \right] \psi_{out}^+ = -\hat{T}\psi_i, \quad (2.13)$$

where ψ_i is the initial state out of which ionization takes place, and \hat{T} denotes the relevant transition operator.

Based on [15, 17], the asymptotic electron probability current density can be written as,

$$J_v(\chi, \varphi) \Big|_{v=v_{det}} \propto \frac{1}{2\pi\chi v\sqrt{\chi^2 + v^2}} \left| \sum_{n_1, m} e^{i(\theta_{n_1, |m|}(v) + \phi_{n_1, |m|})} X_{n_1, |m|}(\chi) e^{im\varphi} d_{n_1, m} \right|^2 \Big|_{v=v_{det}} \quad (2.14)$$

The quantities $d_{n_1, m} = \langle \psi_{n_1, m}^{E, F} | \hat{T} | \psi_i \rangle$ in equation (2.16) denote the transition matrix elements between the initial state ψ_i and the final Stark states $\psi_{n_1, m}^{E, F}$, induced by a number of laser beams. The summation over n_1 formally extends from $n_1 = 0$ to infinity; although, beyond a certain maximum value, the terms in the summation become negligibly small. It turns out that the surviving terms are those satisfying the $0 \leq Z^{n_1, |m|} \leq Z$ inequalities. The m -sum includes all possible values of m , both positive and negative, as permitted by the selection rules.

By integrating $J_v(\chi, \varphi)$ over the surface of the $v = v_{det}$ paraboloid (where the surface element along the χ and φ coordinates is $dS = \chi v \sqrt{\chi^2 + v^2} d\chi d\varphi$) [30], we obtain the total ionization rate, w_{tot} ,

$$w_{tot} = \int J_{v_{det}} dS \propto \sum_{n_1, m} |d_{n_1, m}|^2 \quad (2.15)$$

which is proportional to the incoherent sum over the squared modulus of the excitation matrix elements. The latter contain the laser field amplitudes.

Furthermore, as $v_{det} \rightarrow \infty$ we can make the approximation $\sqrt{\chi^2 + v_{det}^2} \approx v_{det}$ and we arrive at,

$$J_v(\chi, \varphi) \Big|_{v=v_{det}} \propto \frac{1}{\chi} \left| \sum_{n_1, m} e^{i(\theta_{n_1, |m|}(v) + \phi_{n_1, |m|})} X_{n_1, |m|}(\chi) e^{im\varphi} d_{n_1, m} \right|^2 \Big|_{v=v_{det}}. \quad (2.16)$$

as the final form of the current probability density.

2.2 Multielectron atoms

It is essential to extend our discussion to multi-electron atoms, dealing particularly with a highly excited Rydberg electron outside an ionic core. Rydberg atoms are characterized by a valence electron excited to a high n orbital, exhibiting properties that resemble those of hydrogen. This similarity becomes increasingly accurate as the principal quantum number n increases [6]. For the hydrogen atom, the energy levels of the Rydberg states are given by

$$E_n = I_H - \frac{Ryd_H}{n^2} \quad (2.17)$$

where I_H and Ryd_H are the ionization potential and the Rydberg constant of hydrogen atom, respectively. After ignoring spin-orbit coupling, the energy of the valence electron for high- n Rydberg states, is transformed as,

$$E_{n\ell} = I_A - \frac{Ryd_A}{(n - \mu_\ell)^2} \quad (2.18)$$

with I_A and Ryd_A the ionization potential and mass-corrected Rydberg constant of the specific atom. The distinction lies in the presence of the parameter μ_ℓ , known as quantum defect, which arises from the interaction between the excited electron and the ionic core. This interaction is induced either by the penetration of the excited low- ℓ electron wave functions into the ionic core, or by the polarization of the core due to the presence of the high- ℓ Rydberg electrons. Consequently, this interaction causes the Rydberg energy levels to shift relative to their hydrogenic counterparts. The ℓ subscript in μ_ℓ signifies that the quantum defect is strongly dependent on the orbital angular momentum quantum number ℓ while it becomes nearly independent of n close to the ionization limit.

In this work, we are interested in the Rydberg states of Alkali atoms with a single valence electron outside closed (sub)shells. As a result, the Rydberg electron interacts with a spherically symmetric core. It can be demonstrated that for these atoms, the probability current density retains the same form as in Eq.(2.16). However, in regards to the transition matrix elements $d_{n_1, m}$, there are quite important differences from the hydrogenic case. According to the Fano-Harmin Frame Transformation Theory (FTT) [33–35], these matrix elements are modified as follows,

$$d_{n_1, m} = \sum_{\ell} d_{\ell}^m \alpha_{\ell, n_1}^m \quad (2.19)$$

with d_{ℓ}^m the zero-static-field excitation matrix elements that can be evaluated in spherical coordinates. In equation (2.19), the ℓ -sum runs over all the final state values allowed by the selection rule $\Delta\ell = \pm 1$ per absorbed photon. Regarding the factors α_{ℓ, n_1}^m , they are defined by

$$\alpha_{\ell, n_1}^m \equiv \sum_{n'_1} W_{\ell, n'_1}^m B_{n'_1, n_1}^{|m|} \quad (2.20)$$

and their values are contingent upon the elements of the matrices \mathbf{W} and \mathbf{B} [20, 36] that are written as:

$$\mathbf{B}^{|m|} \equiv \left[\mathbf{I} - i\mathbf{R}^{|m|} \right]^{-1} \quad (2.21)$$

$$\mathbf{W}^m \equiv \cos\delta^{-1} [\mathbf{U}^m]^T \left[\mathbf{I} - \cot\gamma^{|m|} \mathbf{K}^{|m|} \right]^{-1}, \quad \mathbf{W}^{-|m|} = (-1)^{|m|} \mathbf{W}^{|m|} \quad (2.22)$$

In equations (2.21) and (2.22), \mathbf{I} is the identity matrix and \mathbf{R} is the reaction matrix,

$$\mathbf{R}^{|m|} = \mathbf{K}^{|m|} \left[\mathbf{I} - \cot\gamma^{|m|} \mathbf{K}^{|m|} \right]^{-1} \quad (2.23)$$

which depends on the matrix \mathbf{K} ,

$$\mathbf{K}^{|m|} = \mathbf{U}^m \tan\delta [\mathbf{U}^m]^T. \quad (2.24)$$

The T superscript in Eq.(2.22) indicates transposition. The connection between the Stark parabolic channels and the spherical, zero-static-field ones is established by the frame transformation matrix \mathbf{U} , which satisfies the symmetry property $\mathbf{U}^{-|m|} = (-1)^{|m|} \mathbf{U}^{|m|}$. Furthermore, the origin of the diagonal matrix $\cot\gamma^{|m|}$ is hydrogenic and reflects the n_1 -specific relative phase $\gamma_{n_1}^{|m|}$ between the hydrogenic regular and irregular Y -wavefunctions for large ν [35]. Lastly, the diagonal matrices, $\cos\delta$ and $\tan\delta$, consists of the phases $\delta_\ell = \pi \cdot \mu_\ell$, where μ_ℓ are the zero-field quantum defects associated with the relevant Rydberg series [34, 37, 38].

For the purely hydrogenic case, the quantum defects are zero, leading to $\mathbf{R} = \mathbf{K} = 0$, and Eq.(2.21) translates to $\mathbf{B} = \mathbf{I}$. In this case, the absence of non-zero off-diagonal elements of the matrix \mathbf{B} indicates no channel mixing. On the other hand, non-zero quantum defects result in non-zero off-diagonal elements in the \mathbf{B} matrix, leading to coupling among the n_1 channels. This channel mixing is evident in Eq.(2.20), and as a result the quantities α_{ℓ, n_1}^m can be broken down into ‘mixing amplitudes’ between a given n_1 channel and all of the n_1' channels [31].

2.3 Matrix Elements in a bichromatic field

The calculation of $J_v(\chi, \varphi)$ in Eq.(2.16) necessitates the evaluation of the corresponding transition matrix elements $d_{n_1, m}$. As outlined in Eq.(2.19), this involves computing the zero-field excitation matrix elements in spherical coordinates. More specifically, in this work, we examine the interaction of non-hydrogenic atoms with a fundamental frequency (ω) laser beam and its mutually coherent second harmonic (2ω), which induces two- and one-photon transitions, respectively, to the final Stark states $\psi_{\ell, m}$. The wave functions and the energy levels of the initial and final states of the specific Alkali atom employed, are calculated using the Schrödinger equation,

$$\left[-\frac{1}{2} \nabla^2 + U(\mathbf{a}_\ell; r) - E \right] \psi(\mathbf{r}) = 0. \quad (2.25)$$

where $U(\mathbf{a}_\ell; r)$ is a spherically symmetric, atom dependent parametric model potential that is obtained from the literature [28].

In the above problem at hand, the transition operator can be described as

$$\hat{T} = \hat{T}_{2\omega}^{(1)} + \hat{T}_{\omega}^{(2)} \quad (2.26)$$

with $\hat{T}_{\omega}^{(1)}$ and $\hat{T}_{2\omega}^{(2)}$ being the one- and two-photon transition operators, respectively, of the two light beams [30]. The two-photon transitions can be described by one-photon ones between the final states $\psi_{\ell,m}$ and a virtual state ψ_ν . The latter is calculated using the Dalgarno-Lewis method [39]. The corresponding differential equation is written as,

$$\left[-\frac{1}{2}\nabla^2 + U(\mathbf{a}_\ell; r) - E_\nu \right] \psi_\nu = -\hat{T}_{\omega}^{(1)} \psi_i, \quad (2.27)$$

with $E_\nu = E_i + \omega = (E + E_i)/2$ the virtual state energy, and $U(\mathbf{a}_\ell; r)$ is the same parametric potential used in Eq.(2.25). With the same reasoning, we may replace $\langle \psi_{\ell,m} | \hat{T}_{\omega}^{(2)} | \psi_i \rangle$ by $\langle \psi_{\ell,m} | \hat{T}_{\omega}^{(1)} | \psi_\nu \rangle$, and finally the zero-field transition matrix elements from the initial or virtual state to the final Stark states $\psi_{\ell,m}$ can be expressed as

$$d_\ell^{m(1)} = \langle \psi_{\ell,m} | \hat{T}_{2\omega}^{(1)} | \psi_i \rangle \quad d_\ell^{m(2)} = \langle \psi_{\ell,m} | \hat{T}_{\omega}^{(1)} | \psi_\nu \rangle. \quad (2.28)$$

In Eqs.(2.28) the single-photon dipole transition operators of the two light beams can be expressed as,

$$\hat{T}_{\omega}^{(1)} = \mathcal{E}_\omega e^{i\Phi_\omega} \boldsymbol{\epsilon}_\omega \cdot \mathbf{r} \quad (2.29)$$

$$\hat{T}_{2\omega}^{(1)} = \mathcal{E}_{2\omega} e^{i\Phi_{2\omega}} \boldsymbol{\epsilon}_{2\omega} \cdot \mathbf{r} \quad (2.30)$$

where $\boldsymbol{\epsilon}_\omega$ and $\boldsymbol{\epsilon}_{2\omega}$ are linear polarization vectors, \mathcal{E}_ω and $\mathcal{E}_{2\omega}$ denote real time-independent amplitudes and Φ_ω , $\Phi_{2\omega}$ are fixed but controllable phases.

Using Eq.(2.19) for non-hydrogenic atoms we obtain the total transition matrix elements,

$$d_{n_1,m} = \sum_\ell d_\ell^{(1)m} \alpha_{\ell,n_1}^m + \sum_{\ell'} d_{\ell'}^{(2)m} \alpha_{\ell',n_1}^m \quad (2.31)$$

where ℓ and ℓ' refer to the allowed final states angular momentum quantum numbers for the one- and two-photon transitions, respectively. Then, by writing the virtual state in the form,

$$\psi_\nu = \mathcal{E}_\omega e^{i\Phi_\omega} \tilde{\psi}_\nu, \quad (2.32)$$

and introducing

$$\eta \equiv \frac{\mathcal{E}_\omega^2}{\mathcal{E}_{2\omega}} \quad \Delta\Phi \equiv 2\Phi_\omega - \Phi_{2\omega} \quad (2.33)$$

further manipulation of Eq.(2.31) leads to,

$$d_{n_1,m} = \mathcal{E}_{2\omega} e^{i\Phi_{2\omega}} \left[\sum_\ell D_\ell^{(1)m} \alpha_{\ell,n_1}^m + \eta e^{i\Delta\Phi} \sum_{\ell'} D_{\ell'}^{(2)m} \alpha_{\ell',n_1}^m \right] \quad (2.34)$$

where,

$$D_\ell^{(1)m} = \langle \psi_{\ell,m} | \boldsymbol{\epsilon}_{2\omega} \cdot \mathbf{r} | \psi_i \rangle \quad D_{\ell'}^{(2)m} = \langle \psi_{\ell',m} | \boldsymbol{\epsilon}_\omega \cdot \mathbf{r} | \tilde{\psi}_\nu \rangle \quad (2.35)$$

are the single- and two-photon transition matrix elements independent of the laser field amplitudes and phases.

The method for calculating the initial, virtual and final state wave functions, as well as the matrix elements $D_\ell^{(1)m}$ and $D_{\ell'}^{(2)m}$ is presented in detail in the Appendix.

2.4 Excitation schemes

We consider first an excitation scheme where the initial state ψ_i is the ground $|n_g, s\rangle$ state of an Alkali metal atom (where $n_g = 2, 3, 4, 5, 6$ refers to Li, Na, K, Rb, and Cs, respectively), characterized by $\ell = 0$ and $m = 0$, as illustrated in Figure (2.3). This is a standard bichromatic $\omega/2\omega$ excitation scheme that has been repeatedly analyzed in previous studies [30, 40, 41], due to its relative simplicity. This scheme may be implemented via the experimental arrangement depicted in Figure 2.2, and includes a photoionization microscope [13, 42]. The latter consists of the repeller, the extractor, and ground electrodes, along with an Einzel lens for image magnification and a two-dimensional PSD. The laser-atom interaction is confined between the repeller and extractor electrodes, where the laser beam(s) intercept an atomic beam consisting of ground state Alkali atoms. The linear polarization of both laser fields (propagating along the x -axis) are aligned parallel to the field direction (z -axis, π -polarization). This configuration imposes the selection rule $\Delta m = 0$ per photon, resulting in $m = 0$ final states. Additionally, the dipole selection rule $\Delta \ell = \pm 1$ permits $\ell = 1$ final states for single-photon transitions and $\ell = 0, 2$ ones for two-photon transitions.

Despite being apparently simple, the PSCC scheme of Figures 2.2 and 2.3 presents certain limitations. Specifically, assuming gaussian laser beams, we may use the relation $w(x) = w_0 \sqrt{1 + (x/x_0)^2}$ for the beam radius, where $w_0 = f\lambda/\pi D$ and $x_0 = \pi w_0^2/\lambda$, are the beam waist and confocal parameter, respectively. In these expressions, f is the focal length of the mirror focusing the two laser beams in the laser-atom interaction region [43], D the beam diameter in this mirror and λ the laser wavelength [44].

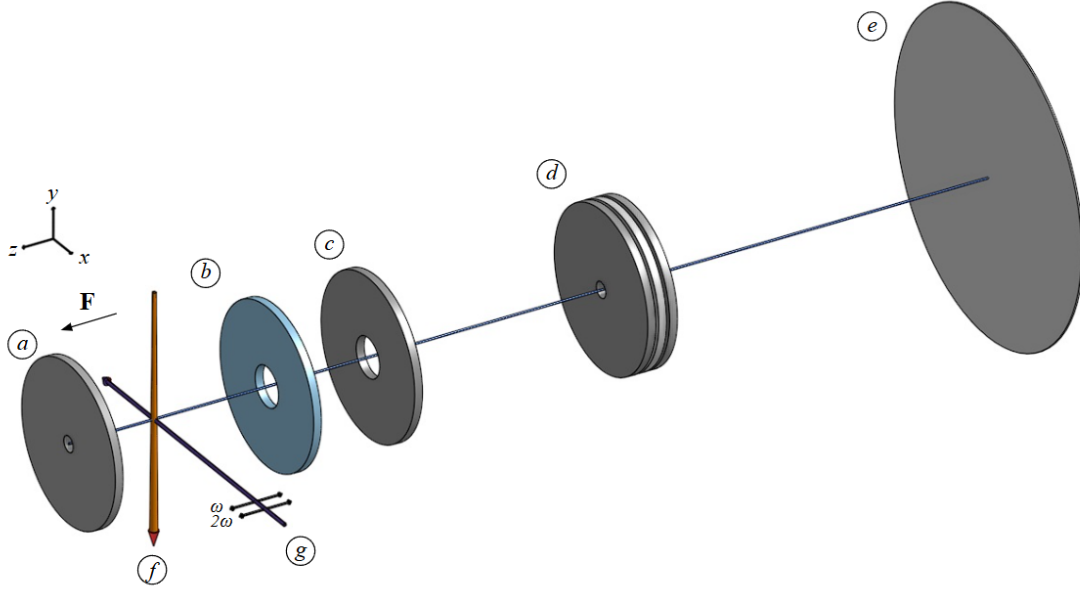


Figure 2.2: Schematic view of the suggested experimental setup, using a photoionization microscope consisting of a VMI spectrometer with the repeller (a), extractor (b), and ground (c) electrodes, a three-element Einzel lens (d), and a PSD (e), along with the atomic beam (f), and control laser beams ($\omega/2\omega$) (g).

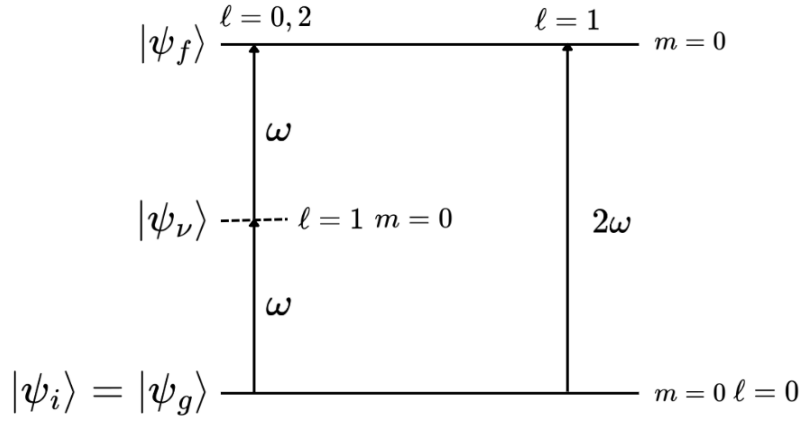


Figure 2.3: One- and two-photon excitation from the $m = 0, \ell = 0$ ground state.

Based on this laser beam profile, and assuming a common diameter D for the two light beams at the focusing mirror, a region is formed between the ω and 2ω (highlighted in blue of Figure 2.4) where these beams do not overlap. This non-overlap leads to the formation of parasitic charges (ions and electrons). The parasitic ions deteriorate the PSCC efficiency of the total signal, while parasitic electrons compromise the control capabilities of the recorded images (differential cross section).

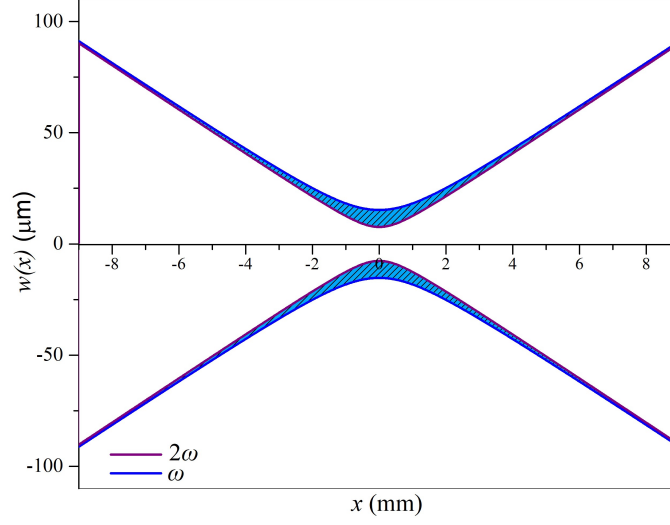


Figure 2.4: Non-overlap region (blue area) using the ω , 2ω laser beams on the excitation scheme of Figure 2.3.

Nevertheless, under these conditions, following from Eq.(2.34) the transition matrix elements are expressed as,

$$d_{n_1,0} = \mathcal{E}_{2\omega} e^{i\Phi_{2\omega}} D_1^{(1)0} \left[\alpha_{1,n_1}^0 + \eta e^{i\Delta\Phi} \Lambda^{(1)} (\alpha_{0,n_1}^0 + \Lambda^{(2)} \alpha_{2,n_1}^0) \right], \quad (2.36)$$

where we have defined the Λ -parameters as,

$$\Lambda^{(2)} \equiv \frac{D_2^{(2)0}}{D_0^{(2)0}} \quad \Lambda^{(1)} \equiv \frac{D_0^{(2)0}}{D_1^{(1)0}}. \quad (2.37)$$

With the matrix elements now defined, the electron probability current density, as defined in Eq.(2.16), is written as,

$$J_{v_{det}}(\chi) \propto \frac{1}{\chi} \left| \sum_{n_1} \left[\alpha_{1,n_1}^0 + \eta e^{i\Delta\Phi} \Lambda^{(1)} (\alpha_{0,n_1}^0 + \Lambda^{(2)} \alpha_{2,n_1}^0) \right] e^{i(\theta_{n_1,0} + \phi_{n_1,0})} X_{n_1,0}(\chi) \right|^2. \quad (2.38)$$

In order to overcome the limitations discussed above, we have examined another bichromatic excitation scheme where the initial state ψ_i is the lower excited state of an Alkali metal atom. Thus, the initial $\psi_i = |n_g p\rangle$ state is characterized by quantum numbers $\ell = 1$ and $|m| = 1$, as shown in Figure 2.5. To prepare the system in this initial state, we use an excitation laser beam which propagates along the negative z -axis and whose linear polarization is perpendicular to the static field direction (σ -polarization). This is implemented as shown in Figure 2.6. This enforces the selection rule $|\Delta m| = 1$. Further, the $\Delta m = 0$ dipole selection rule for the bichromatic laser fields (linear polarizations aligned parallel to \mathbf{F}), results in final

states that are restricted to $|m| = 1$ and $\ell = 2$ for the single-photon transition, while for the two-photon transition the final states have $\ell = 1, 3$.

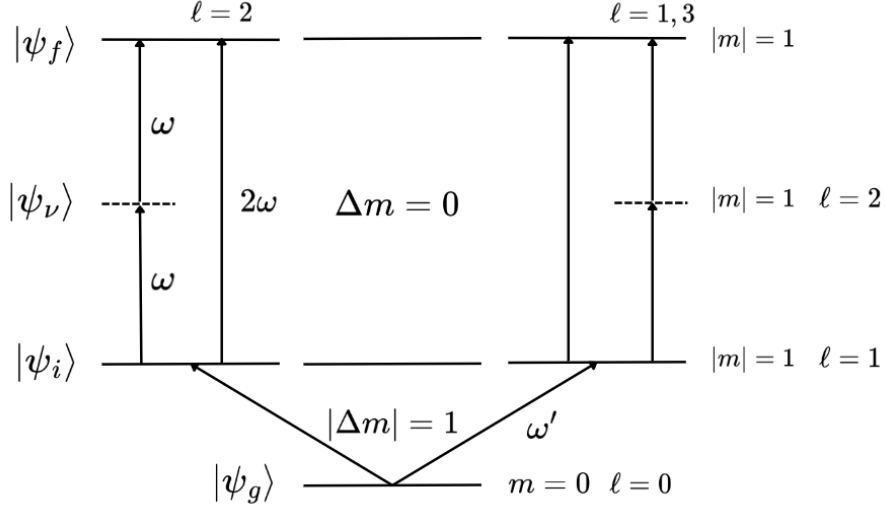


Figure 2.5: One- and two-photon excitation from the initial state with $\ell = 1$ and $|m| = 1$.

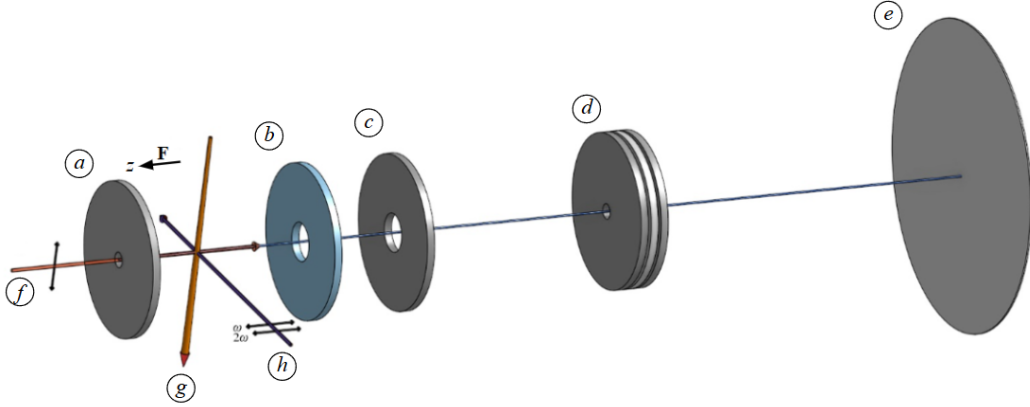


Figure 2.6: Schematic view of the suggested experimental setup, using a photoionization microscope consisting of a VMI spectrometer with the repeller (a), extractor (b), and ground (c) electrodes, a three-element Einzel lens (d), and a PSD (e), along with the excitation laser (f), the atomic beam (g) and control laser beams ($\omega/2\omega$) (h).

This excitation scheme addresses the drawbacks of the one analyzed previously by restricting the laser-atom interaction to a smaller region where all three laser

beams overlap (gray area in Figure 2.7), thus preventing the formation of charged particle signals. Additionally, the small overlap region is compatible with the VMI spectrometer operation. This excitation scheme probes $m > 0$ final Stark states, which are less core penetrating and consequently closer to the hydrogenic case.

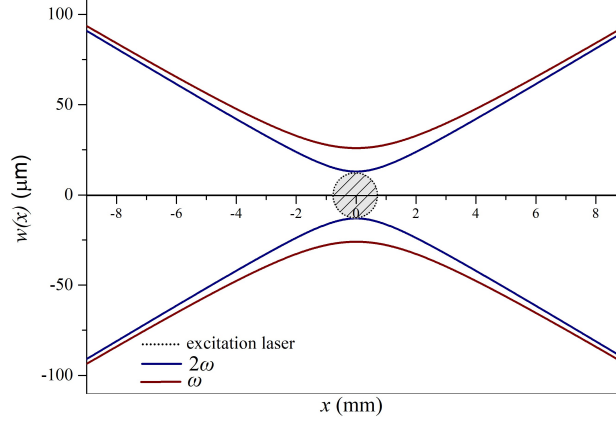


Figure 2.7: Interaction region (gray area) of the excitation scheme of Figures 2.5 and 2.6.

In this case, the transition matrix elements of Eq.(2.34) are expressed as

$$d_{n_1, \pm 1} = \mathcal{E}_{2\omega} e^{i\Phi_{2\omega}} D_2^{(1)1} \left[\alpha_{2, n_1}^{\pm 1} + \eta e^{i\Delta\Phi} \Lambda^{(1)} (\alpha_{1, n_1}^{\pm 1} + \Lambda^{(2)} \alpha_{3, n_1}^{\pm 1}) \right], \quad (2.39)$$

where the Λ parameters are defined as,

$$\Lambda^{(1)} \equiv \frac{D_1^{(2)1}}{D_2^{(1)1}} \quad \Lambda^{(2)} \equiv \frac{D_3^{(2)1}}{D_1^{(2)1}}. \quad (2.40)$$

Note that, the electron probability current density from Eq.(2.16) includes only two terms in the m -summation, corresponding to $m = 1$ and $m = -1$. The matrix elements $d_{n_1, -1}$ and $d_{n_1, 1}$ are related by $d_{n_1, -1} = -d_{n_1, 1}$, following the definition of the alpha factors in Eq.(2.20). The latter depend on the \mathbf{W} matrix which exhibits the property $W^{-|m|} = (-1)^{|m|} W^{|m|}$, as outlined in Eq.(2.22). This affects the summation over the possible m values, resulting in the following expression for the probability current density,

$$J_{v_{det}}(\chi, \varphi) \propto \frac{\sin^2 \varphi}{\chi} \left| \sum_{n_1} d_{n_1, 1} e^{i(\theta_{n_1, 1} + \phi_{n_1, 1})} X_{n_1, 1}(\chi) \right|^2. \quad (2.41)$$

Then, substituting the definition of $d_{n_1, 1}$ from Eq.(2.39) we derive the final form for the electron probability current density in the excitation of Figure 2.5,

$$J_{v_{det}}(\chi, \varphi) \propto \frac{\sin^2 \varphi}{\chi} \left| \sum_{n_1} \left[\alpha_{2, n_1}^1 + \eta e^{i\Delta\Phi} \Lambda^{(1)} (\alpha_{1, n_1}^1 + \Lambda^{(2)} \alpha_{3, n_1}^1) \right] e^{i(\theta_{n_1, 1} + \phi_{n_1, 1})} X_{n_1, 1}(\chi) \right|^2 \quad (2.42)$$

The above equation explicitly shows the $\sin^2 \varphi$ angular distribution of $J_{v_{det}}$ (while the radial distribution is given by its χ -dependence). This angular distribution is anticipated to exhibit a nodal line along the horizontal χ -axis as a distinct feature.

2.5 Contrast and Optimization

Assuming perfect overlap between the two light beams, the efficiency of the PSCC approach for a given observable Ω is determined by the achieved contrast V^Ω ,

$$V^\Omega = \frac{\Omega^+ - \Omega^-}{\frac{1}{2}(\Omega^+ + \Omega^-)} \quad (2.43)$$

where Ω^+ and Ω^- represent the values of the observable when the phase difference is $\Delta\Phi = 0$ and $\Delta\Phi = \pi$, respectively. According to this definition the maximum value of the contrast, $|V^\Omega|$, is 2. This maximum occurs when either Ω^+ or Ω^- equals zero [30].

To achieve the optimum absolute contrast value, $|V_{opt}^\Omega|$, we apply the condition $dV^\Omega/d\eta = 0$ which provides the value of η_{opt} for the given observable. Substituting η_{opt} into Eq.(2.43) yields the optimum contrast, V_{opt}^Ω . This condition turns out to be $\Omega^{(1)} = \Omega^{(2)}$ [17, 40, 41], indicating that optimum contrast is achieved when the individual one-photon and two-photon excitation contributions to the observable Ω are equal [30, 41]. However, if either $\Omega^{(1)}$ or $\Omega^{(2)}$ is equal to zero, the observable cannot be controlled.

Applying the above considerations, and using the total excitation rate, $\Omega = w_{tot}$, as the observable, we focus on excitations that lead to the same (and preferably single) m final states values, as described in Section 2.4. Using Eqs.(2.15) and (2.34) we derive the following expression for the ionization rate

$$w_{tot} \propto \sum_{n_1} \left| \sum_{\ell} D_{\ell}^{(1)m} \alpha_{\ell, n_1}^m + \eta e^{i\Delta\Phi} \sum_{\ell'} D_{\ell'}^{(2)m} \alpha_{\ell', n_1}^m \right|^2 \quad (2.44)$$

Note that, the implementation of a PSCC scheme for the total ionization rate, w_{tot} , achieved via simultaneous one- and two-photon atomic excitation, requires the presence of a static electric field (which is not the case for the total cross section) [40, 41]. Setting $\Delta\Phi = 0$ and $\Delta\Phi = \pi$ we obtain w_{tot}^+ and w_{tot}^- , respectively. Substituting these into the contrast definition provided in Eq.(2.43) and applying the optimization condition, $dV^{w_{tot}}/d\eta = 0$, we determine the optimum contrast value:

$$V_{opt}^{w_{tot}} = 2 \frac{\sum_{n_1} \text{Re} \left[\sum_{\ell} D_{\ell}^{(1)m} \alpha_{\ell, n_1}^m (\sum_{\ell'} D_{\ell'}^{(2)m} \alpha_{\ell', n_1}^m)^* \right]}{\left[\sum_{n_1} \left| D_{\ell}^{(1)m} \alpha_{\ell, n_1}^m \right|^2 \sum_{n_1} \left| \sum_{\ell'} D_{\ell'}^{(2)m} \alpha_{\ell', n_1}^m \right|^2 \right]^{1/2}} \quad (2.45)$$

However, as indicated by the above equation, although the equality $w_{tot}^{(1)} = w_{tot}^{(2)}$ can be used as a guideline for attaining the highest possible contrast, it does not necessarily result in the aforementioned maximum contrast value of 2.

Following the same computational steps and using the probability current density as the observable, $\Omega = J_{v_{det}}$, along with Eqs.(2.16) and (2.34), we derive the following expression for V_{opt} ,

$$V_{opt}^{J_{v_{det}}}(\chi) = 2 \frac{\text{Re}[A(\chi)B^*(\chi)]}{|A(\chi)||B(\chi)|} \quad (2.46)$$

with $A(\chi)$ and $B(\chi)$ defined here as,

$$A(\chi) \equiv \sum_{n_1, m} e^{i(\theta_{n_1, |m|}(v_{det}) + \phi_{n_1, |m|})} X_{n_1, |m|}(\chi) e^{im\varphi} \sum_{\ell'} D_{\ell'}^{(2)m} \alpha_{\ell', n_1}^m \quad (2.47)$$

$$B(\chi) \equiv \sum_{n_1, m} e^{i(\theta_{n_1, |m|}(v_{det}) + \phi_{n_1, |m|})} X_{n_1, |m|}(\chi) e^{im\varphi} \sum_{\ell} D_{\ell}^{(1)m} \alpha_{\ell, n_1}^m \quad (2.48)$$

The above equations reveal that, for a given energy E and field strength F , both the magnitude and sign of the optimum contrast, V_{opt} , can vary along the radial coordinate ρ (as $\rho \propto \chi$). Consequently, each radial position within $J_{v_{det}}$ may exhibit different V_{opt} values, making it challenging to achieve uniform control across the entire image.

3 | Results and Discussion

3.1 PSCC just above the saddle point energy

For both excitation schemes outlined in Section 2.4, we conducted a comprehensive analysis of PSCC using sodium (Na) target atoms under different electric field strengths. Sodium was chosen due to its atomic number ($Z = 11$), which is close to that of Mg, a system previously investigated in experiments that revealed faint resonant features with considerable difficulty [19]. Our study dealt with field strengths ranging from 900 V/cm to 1 kV/cm, and just above the saddle point energy, E_{sp} . The choice on the energy range was motivated by the reduced number of continua in this vicinity, facilitating the easier elimination of continuum excitation via PSCC [41]. Within this energy range, interesting avoided crossings were spotted, further supporting the reasoning of decoupling the resonance from the degenerate continua in their neighborhood [13]. Within this energy range and field strengths, we evaluated the total cross section for one-photon ionization, $\sigma^{(1)} = w^{(1)}/\tilde{I}$ (\tilde{I} denoting the intensity per photon energy) where interactions between resonances are evident. Note that, the resonant line shapes for one- and two-photon ionization may differ but the locations of avoided crossings remain practically the same. Of course, control over the total cross section requires the knowledge of the two-photon counterpart as well.

3.1.1 $m = 0$ final Stark states

For the excitation scheme illustrated in Figure 2.3, our analysis focused on the energy range from -182.5 cm^{-1} to -177.0 cm^{-1} , with electric field strengths spanning from 915 V/cm to 980 V/cm with 5 V/cm intervals. Within this energy range, we evaluated the total cross-section for one-photon transitions, $\sigma_{tot}^{(1)}$, as shown in Figure 3.1. Three resonances are clearly visible in this Figure, with the two prominent ones coming into close proximity at around 940–950 V/cm, before diverging again as the electric field increases. This intricate behavior is further highlighted in Figure 3.2, where the energy of each resonance, corresponding to the maximum of the spectral line, is plotted as a function of the electric field strength.

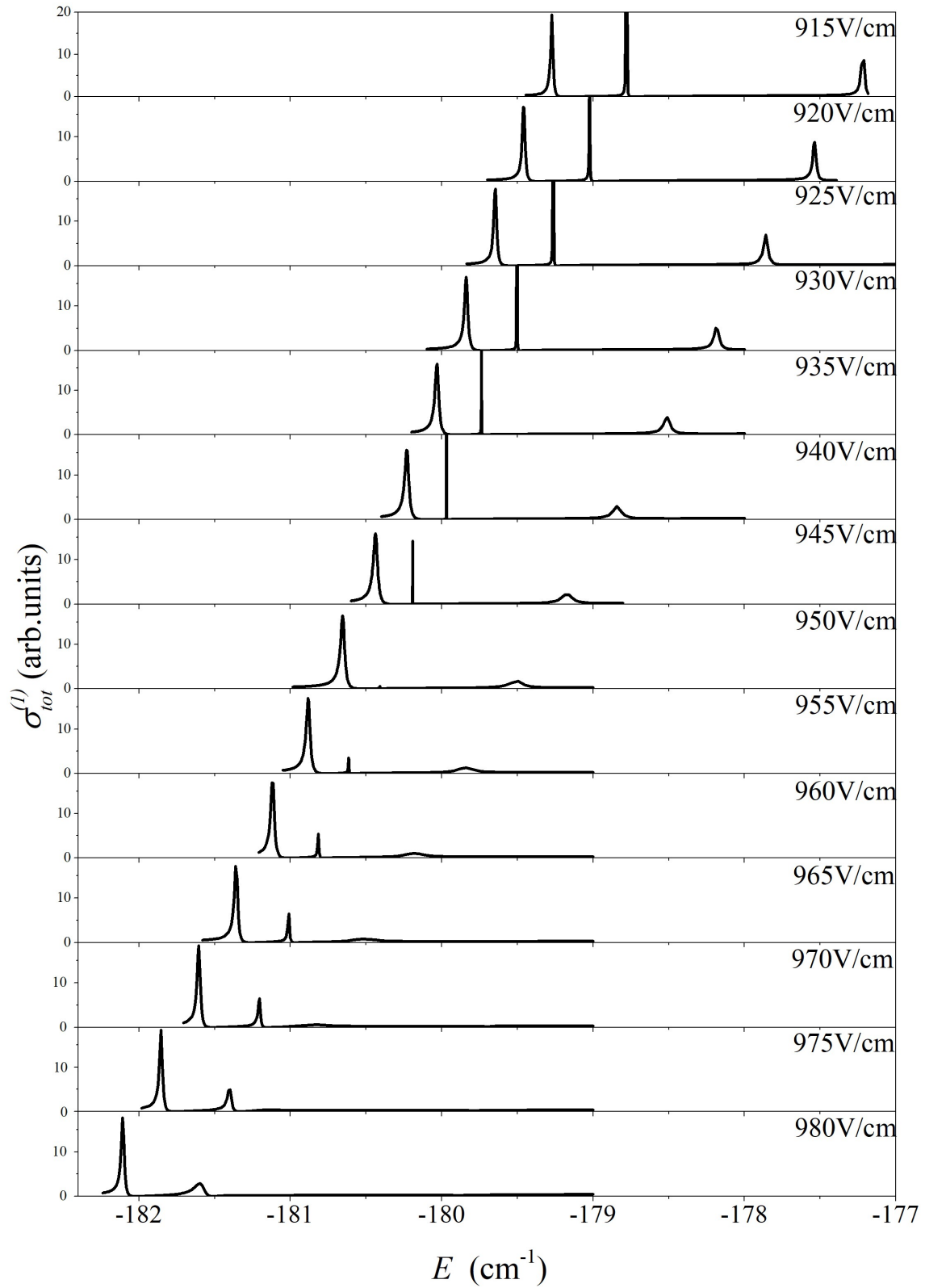


Figure 3.1: Total cross section $\sigma_{tot}^{(1)}$ evaluated for one-photon ionization out of the ground state in the energy range $(-182.5, -177.0)$ cm^{-1} for electric field strengths varying from 915 V/cm to 980 V/cm for the $m = 0$ scenario of Figure 2.3.

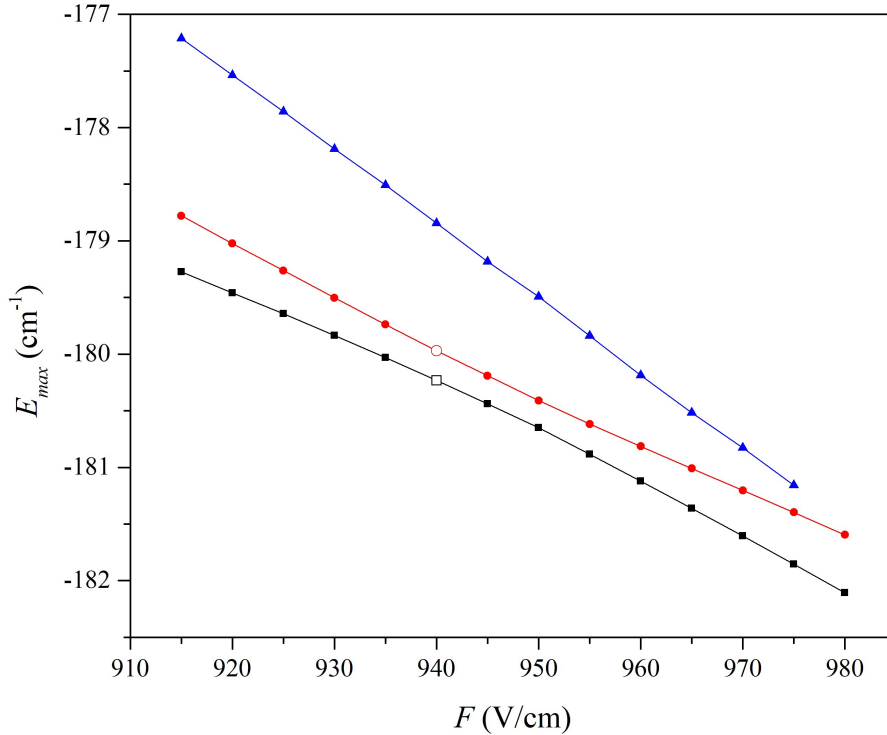


Figure 3.2: Energy of the spectral line maxima of the three resonances at each field of Figure 3.1. The two resonances under study are marked with hollow symbols.

In Figure 3.2, it is evident that the third resonance appears to approach the other two as the field increases. Visual inspection of this Figure supports the claim that, at 980 V/cm the last two resonances have merged with each other, and thus it is not possible to extract the energy of the spectral line maximum for the last resonance. This is indicated by a missing value at 980 V/cm of the blue line in Figure 3.2.

We extended our evaluations to the two resonances at 940 V/cm, with energies -180.232 cm^{-1} and -179.969 cm^{-1} , which translates to the reduced energy values based on Eq.(2.3), $\varepsilon = -0.96023$ and $\varepsilon = -0.95884$, respectively. These energies are also highlighted in Figure 3.2 for this specific field. Utilizing the analysis of Chapter 2, with the optimization condition of Eq.(2.5), we evaluated $V_{opt}(\chi)$ in this field strength for the energies of these two resonances, depicted in Figure 3.3. This figure clearly demonstrates that, for these energies, $V_{opt}(\chi)$ shows no sign changes, thereby making control over the images viable.

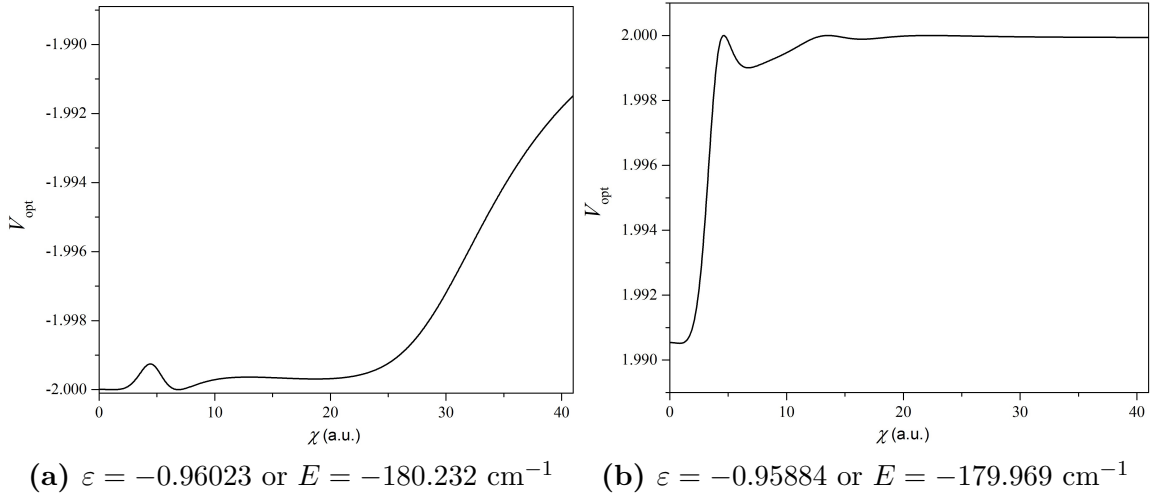


Figure 3.3: Optimum contrast V_{opt} as a function of χ for the resonances at 940 V/cm in the $m = 0$ scenario of Figures 2.3 and 2.2.

Specifically, for the resonance with energy $\varepsilon = -0.96023$ we calculated the probability current density, defined in Eq.(2.16), for one- and two-photon transitions, separately, depicted in Figure 3.4. Then using the $\omega/2\omega$ excitation scheme for $\Delta\Phi = 0$ and $\Delta\Phi = \pi$, we applied the optimization condition to determine the optimum value of η at a specific χ -radius, which for this resonance was calculated at $\chi = 6.81$ a.u., to enhance the resonant feature of the images. The relevant images are depicted in Figure 3.5.

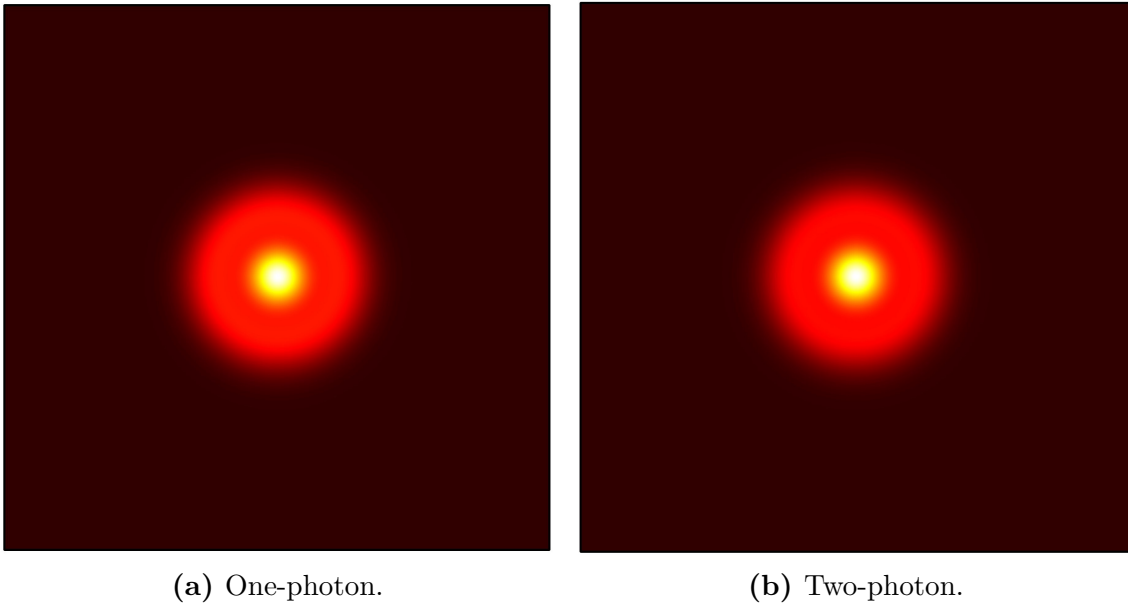


Figure 3.4: $m = 0$: Ionization for the resonance with $\varepsilon = -0.96023$ at 940 V/cm.

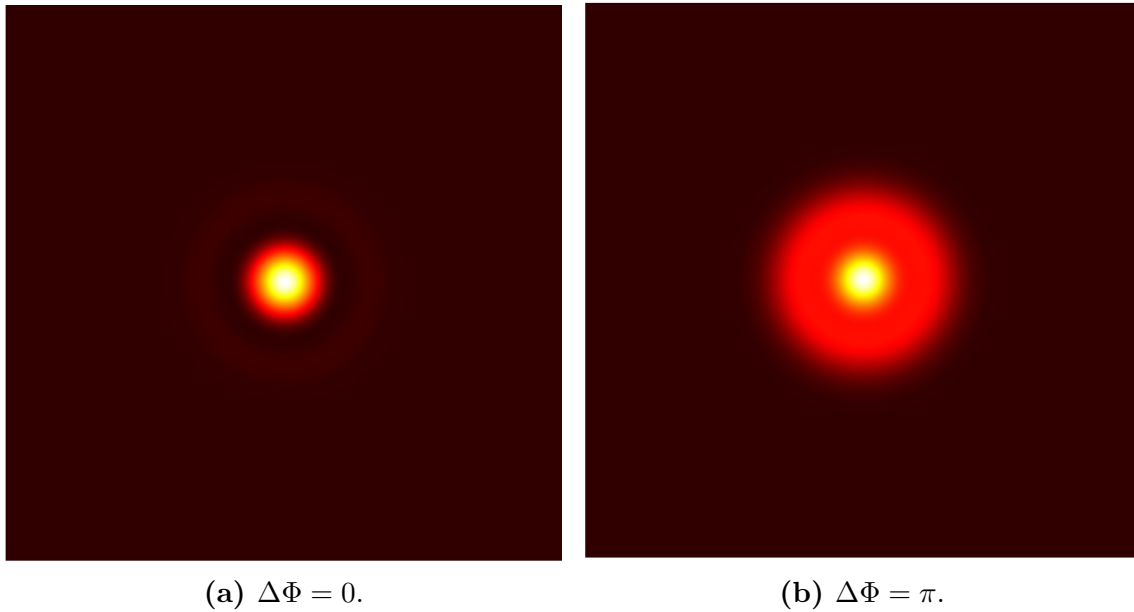


Figure 3.5: $m = 0$: $\omega/2\omega$ control for the resonance with $\varepsilon = -0.96023$ at 940 V/cm.

The respective images for the resonance with $\varepsilon = -0.95884$ are presented in Figure 3.6 and 3.7.

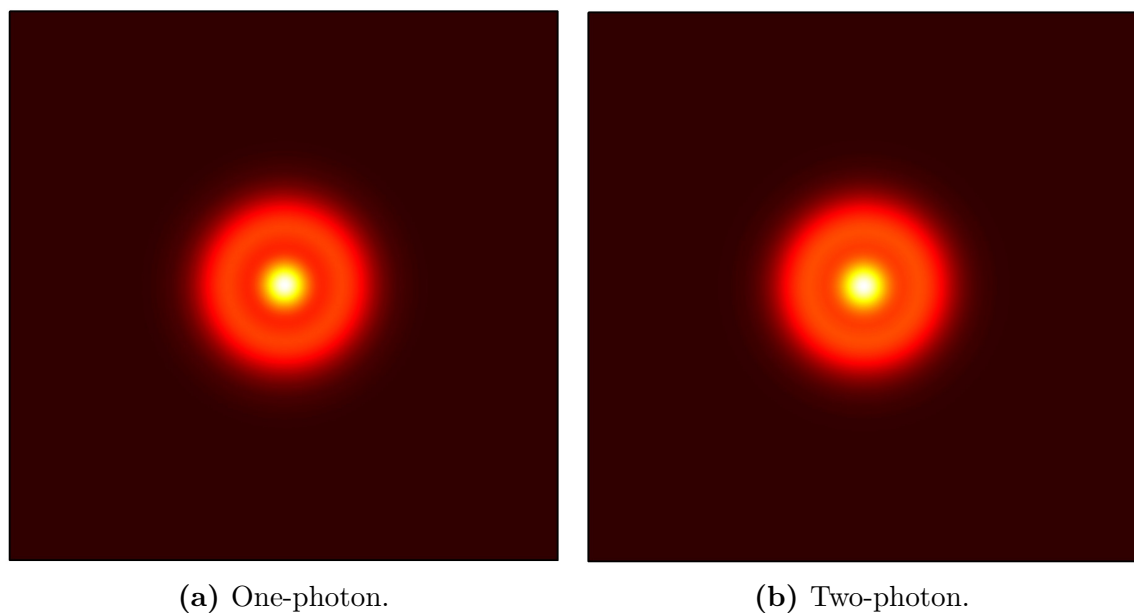


Figure 3.6: $m = 0$: Ionization for the resonance with $\varepsilon = -0.95884$ at 940 V/cm.

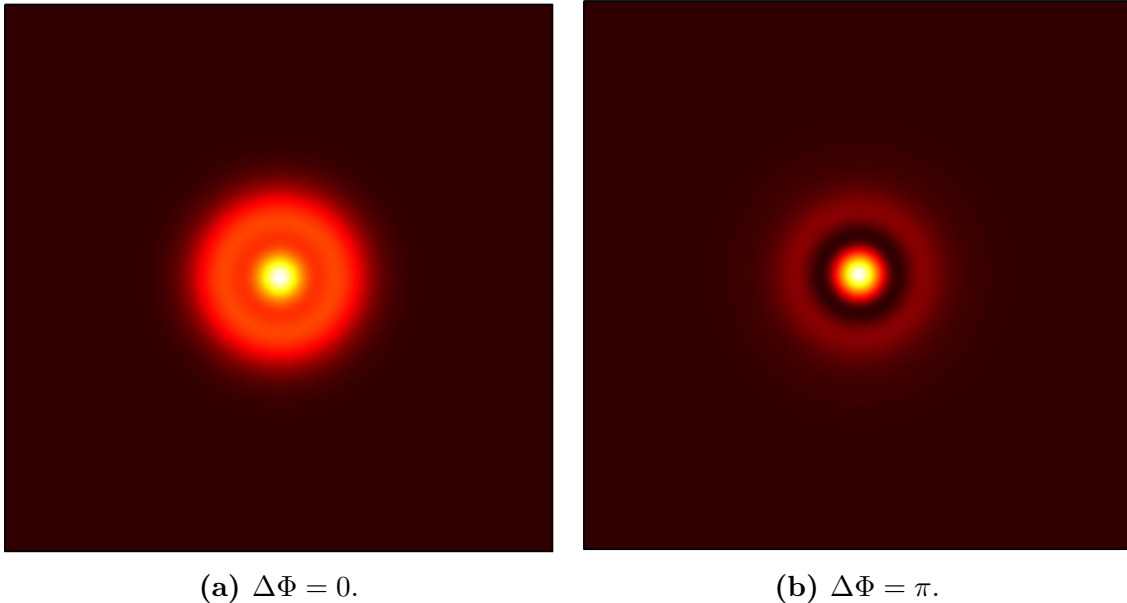


Figure 3.7: $m = 0$: $\omega/2\omega$ control at $\chi = 3.96$ a.u. for the resonance with $\varepsilon = -0.95884$ at 940 V/cm.

It is evident, particularly for the resonance at $\varepsilon = -0.95884$, that while the single and two photon transitions individually showed no differences, the $\omega/2\omega$ did. However, in these cases it was not possible to enhance the resonant features. This may be attributed to the fact that for both of these resonances the interacting continuum states are two, one with $n_1 = 0$ and one with $n_1 = 1$.

3.1.2 $|m| = 1$ final Stark states

Continuing our study of the excitation scheme described in Section 2.4 and illustrated in Figure 2.5, we performed a detailed analysis for the same target atom (Na) under electric fields ranging from 920 V/cm to 990 V/cm. Our study focused on an avoided crossing within the energy range of -184.5 cm^{-1} to -178.0 cm^{-1} , a region selected just above the E_{sp} . In this range, we evaluated the total cross-section for one photon transitions, $\sigma_{tot}^{(1)}$, as shown in Figure 3.8, revealing intricate resonance interactions. Notably, three distinct resonances were identified in this avoided crossing, with the third one traversing the other two as the electric field increases. This behavior becomes particularly pronounced beyond 960 V/cm, with the third resonance overlapping the second one and cannot be distinguished separately, as highlighted in the magnified section of Figure 3.8. Figure 3.9 illustrates the energy corresponding to the maximum of the spectral lines of each of the three resonances, with the exception of the resonance at 970 V/cm (indicated by a gap in the blue line). It can be observed from Figures 3.8 and 3.9 that the first two resonances exhibit their closest separation at 935 V/cm.

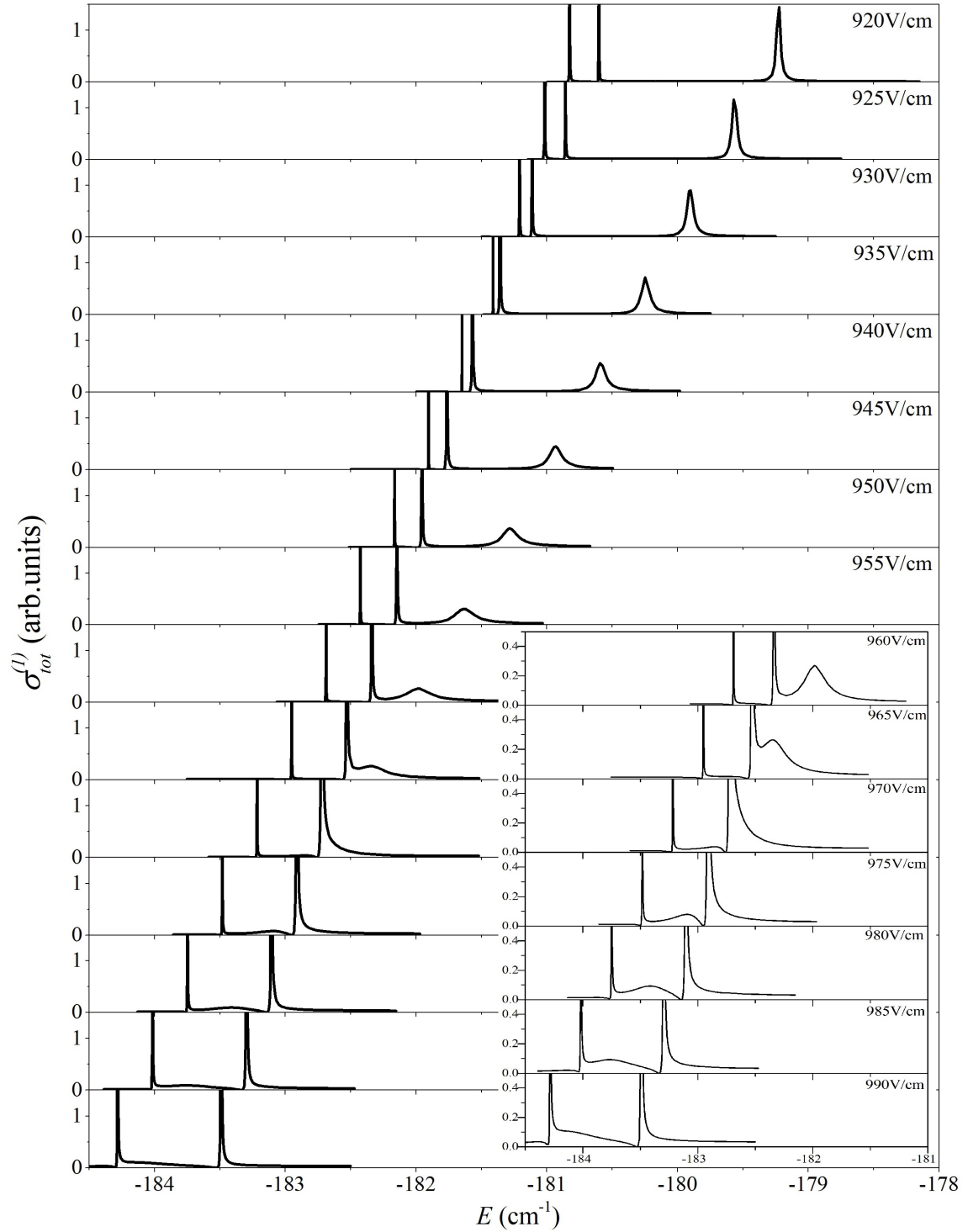


Figure 3.8: Total cross section $\sigma_{tot}^{(1)}$ evaluated for one photon transitions in the energy range $(-184.5, -178.0)$ cm^{-1} for electric field strengths varying from 920 V/cm to 990 V/cm for the $m = 1$ case.

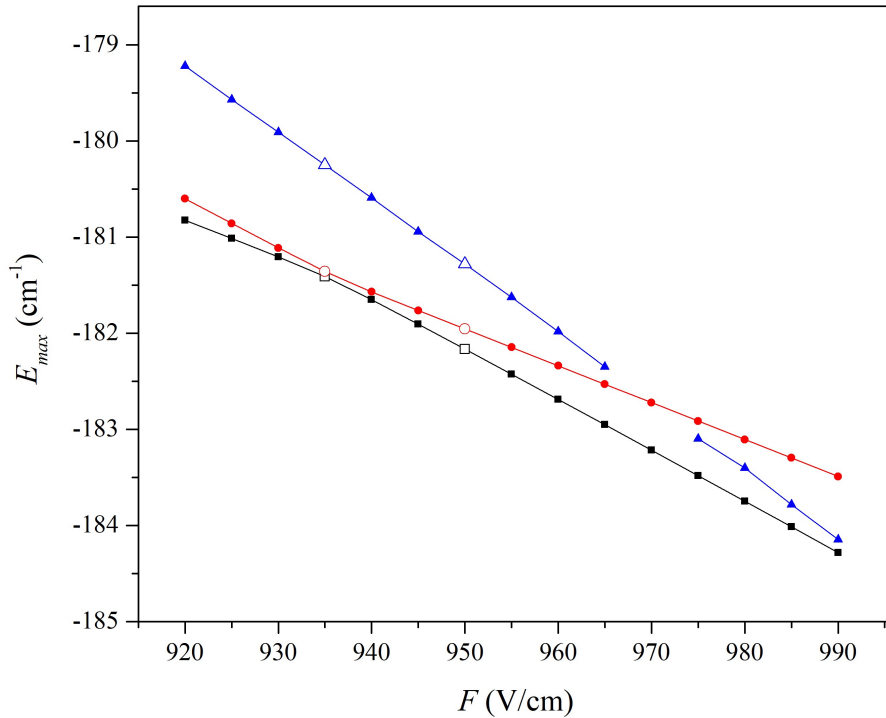


Figure 3.9: Energy of the spectral line maxima of the three resonances at each field for the $|m| = 1$ scenario of Figure 2.5.

Our study particularly focused on two specific electric field strengths: 935 V/cm, where the two resonances exhibit their closest approach, and 950 V/cm, where these resonances are fairly distant. For each resonance at these fields, we calculated the probability current density, as defined in Eq.(2.42), separately for single- and two-photon transitions. Then using the $\omega/2\omega$ excitation scheme for $\Delta\Phi = 0$ and $\Delta\Phi = \pi$, we applied the optimization condition to determine the optimum value of η at specific radius χ to enhance the depiction of resonant features.

We evaluated V_{opt} as a function of χ , as it was defined in Eq.(2.46), for these two electric field strengths and resonant energies to study its behavior. Our analysis revealed that $V_{opt}(\chi)$ remains relatively stable and consistent, exhibiting no sign changes and maintaining nearly constant values in the vicinity of the resonances, approaching the maximum theoretical value of 2. This stability is presented in Figure 3.10, which demonstrates the behavior of $V_{opt}(\chi)$ for two resonances at their respective fields.

3.1. PSCC just above the saddle point energy Chapter 3. Results and Discussion

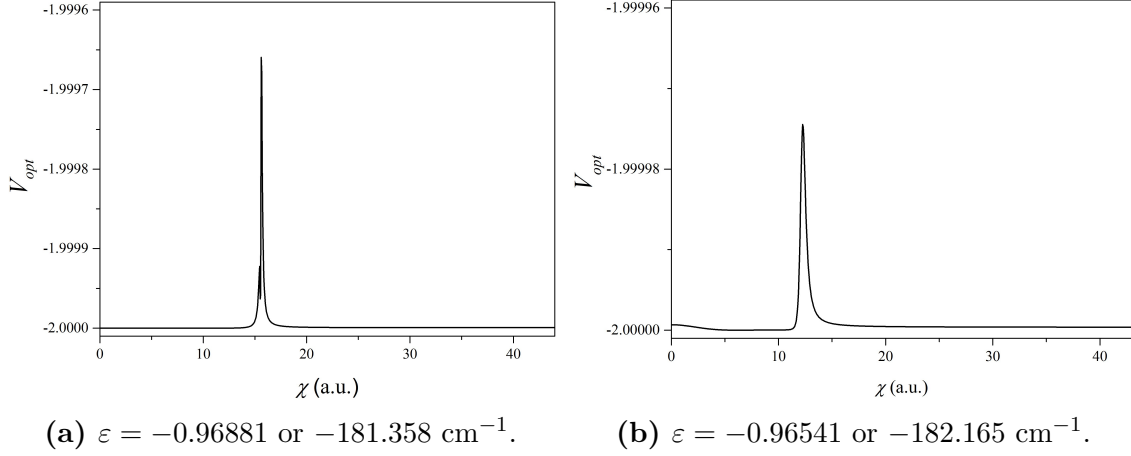


Figure 3.10: Optimum contrast V_{opt} as a function of χ in the $m = 1$ case at (a) 935 and (b) 950 V/cm.

Specifically, at 935 V/cm the energies of the first two resonances are -181.412 cm^{-1} ($\varepsilon = -0.9691$) and -181.358 cm^{-1} ($\varepsilon = -0.96881$). For this resonance, we evaluated $J^{(1)}$ and $J^{(2)}$ for one- and two-photon transitions separately and then applied the optimization condition $J^{(1)} = J^{(2)}$. This condition was met precisely at two radii, as seen in Figure 3.11, but we applied our evaluations at $\chi = 9.91$ a.u as marked in Figure 3.11(a).

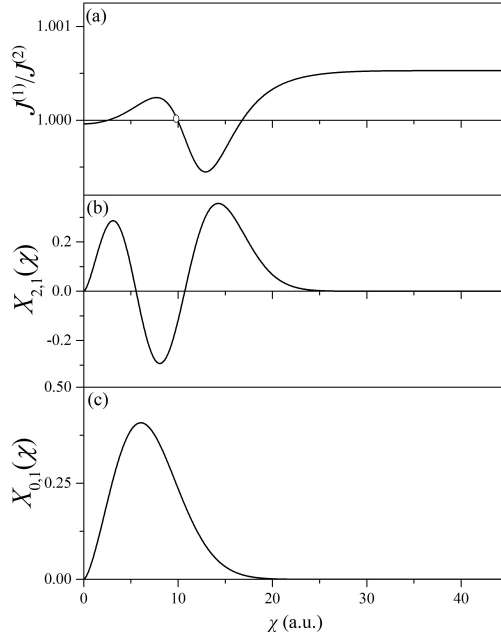


Figure 3.11: (a) Optimization condition along the radius for $\chi = 9.91$. (b) The target state with $n_1 = 2$. (c) The continuum state with $n_1 = 0$.

For the resonance with $\varepsilon = -0.9691$, the images corresponding to the one- and two-photon transitions evaluated separately, are presented in Figure 3.12.

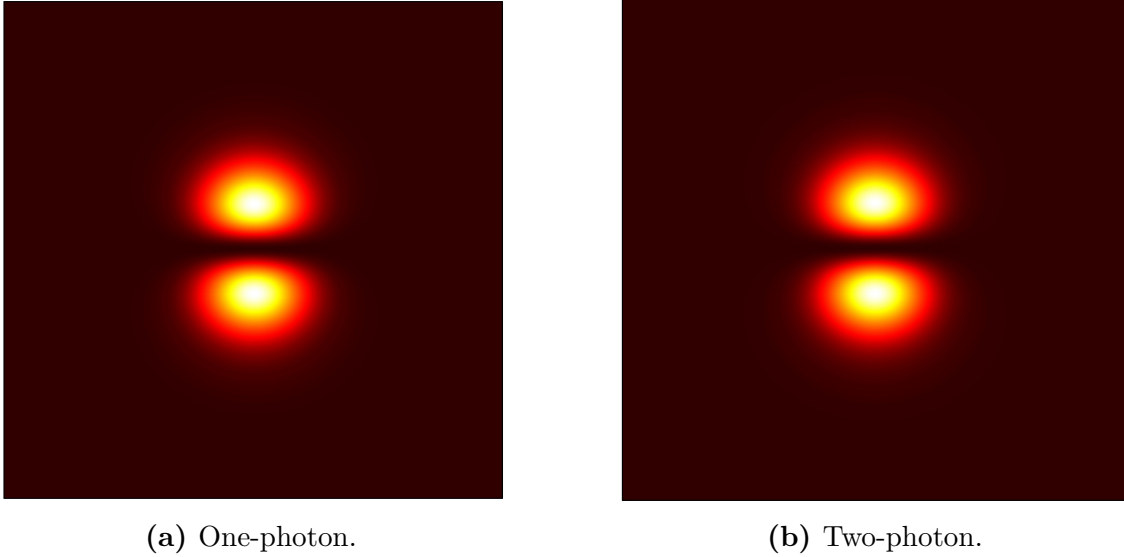


Figure 3.12: Ionization for the resonance with $\varepsilon = -0.9691$ at 935 V/cm.

The relative $\omega/2\omega$ images, evaluated for $\Delta\Phi = 0$ and $\Delta\Phi = \pi$ are shown in Figure 3.13. For $\varepsilon = -0.9691$, two nodes are observed in the images below, indicating that the targeted state has $n_1 = 2$, which is only evident with $\Delta\Phi = 0$. For this energy, there is only one continuum state, with $n_1 = 0$, interacting with this resonance.

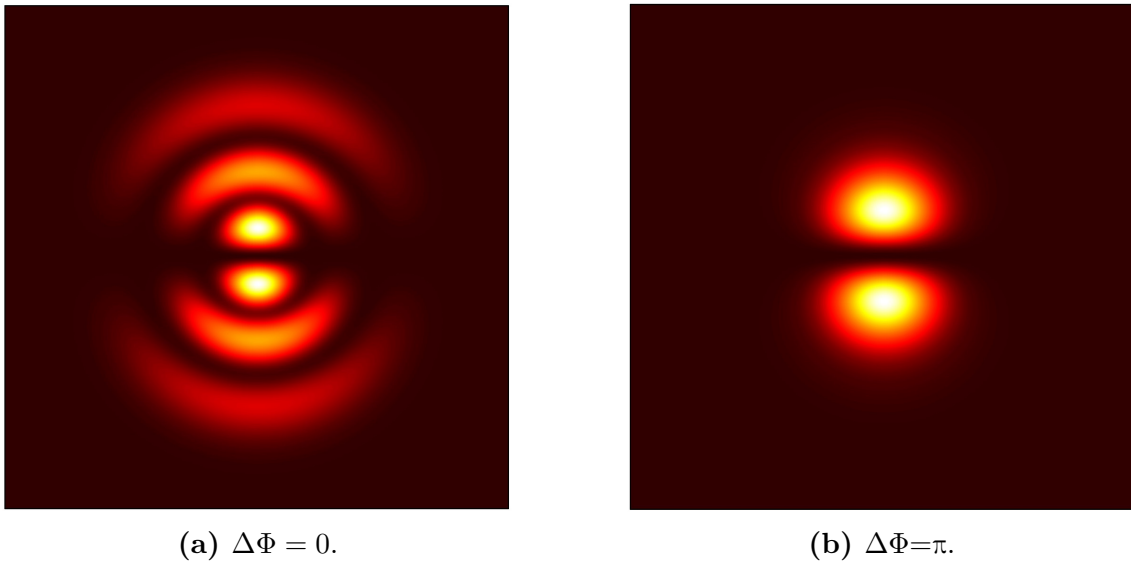


Figure 3.13: Control for the resonance with $\varepsilon = -0.9691$ at 935 V/cm.

It is clear that by applying the optimization condition and adjusting the relative

3.1. PSCC just above the saddle point energy Chapter 3. Results and Discussion

phase between the two laser fields, the resonant characteristics can be effectively revealed.

The same process was applied for the resonance with $\varepsilon = -0.96881$ using the optimization condition at $\chi = 6.81$ a.u. (Figure 3.14).

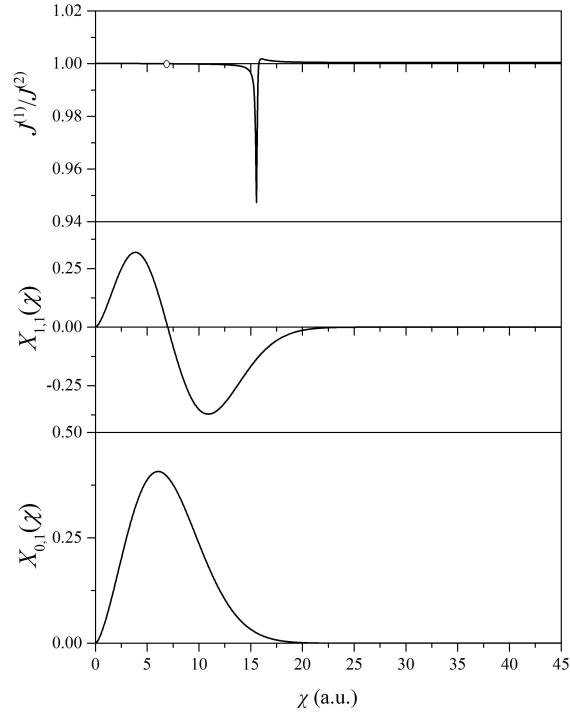


Figure 3.14: (a) Optimization condition at $\chi = 6.81$ a.u. along with the (b) target ($n_1 = 1$) and (c) continuum ($n_1 = 0$) state.

The evaluated images corresponding to the one- and two-photon transitions, are depicted in Figure 3.15 and , the relative $\omega/2\omega$ evaluated images can be seen in Figure 3.16. At this energy, based on the number of nodes, it is evident that the target state has $n_1 = 1$, while the only continuum state has $n_1 = 0$.

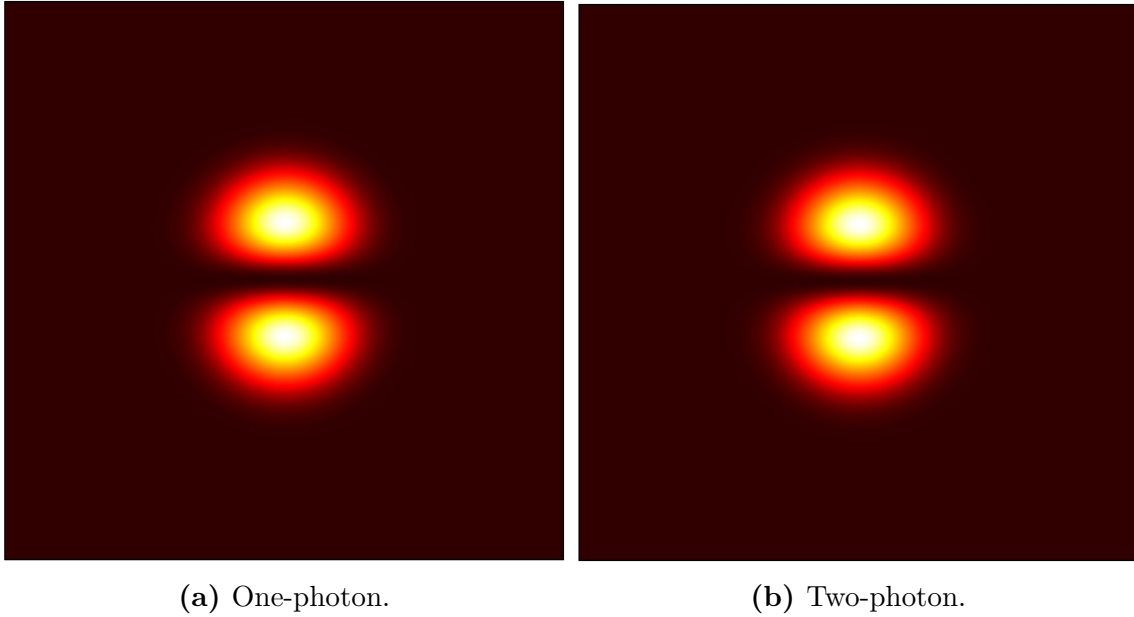


Figure 3.15: Ionization for the resonance with energy $\varepsilon = -0.96881$ at 935 V/cm.

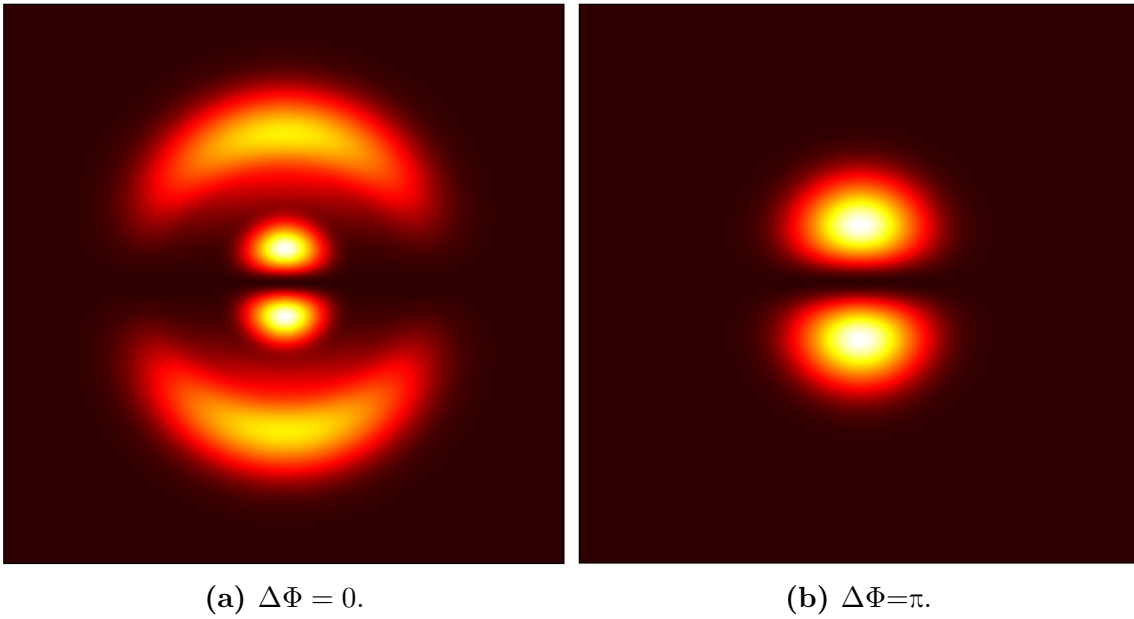


Figure 3.16: Control at $\chi = 6.81$ a.u. for the resonance with $\varepsilon = -0.96881$ at 935 V/cm.

The same process was applied to the three resonances at 950 V/cm with energies $\varepsilon = -0.96541$, $\varepsilon = -0.96429$ and $\varepsilon = -0.96073$. For the first resonance it is evident that the target state has $n_1 = 2$, while for the other resonances the target state has $n_1 = 1$. For all three resonances at this field there is only one continuum state $n_1 = 0$

3.1. PSCC just above the saddle point energy Chapter 3. Results and Discussion

As in the previous field, the images for separate one- and two-photon transition of the first two energies are shown in Figures 3.17 and 3.19, while the $\omega/2\omega$ ones are presented in Figures 3.18 and 3.20.

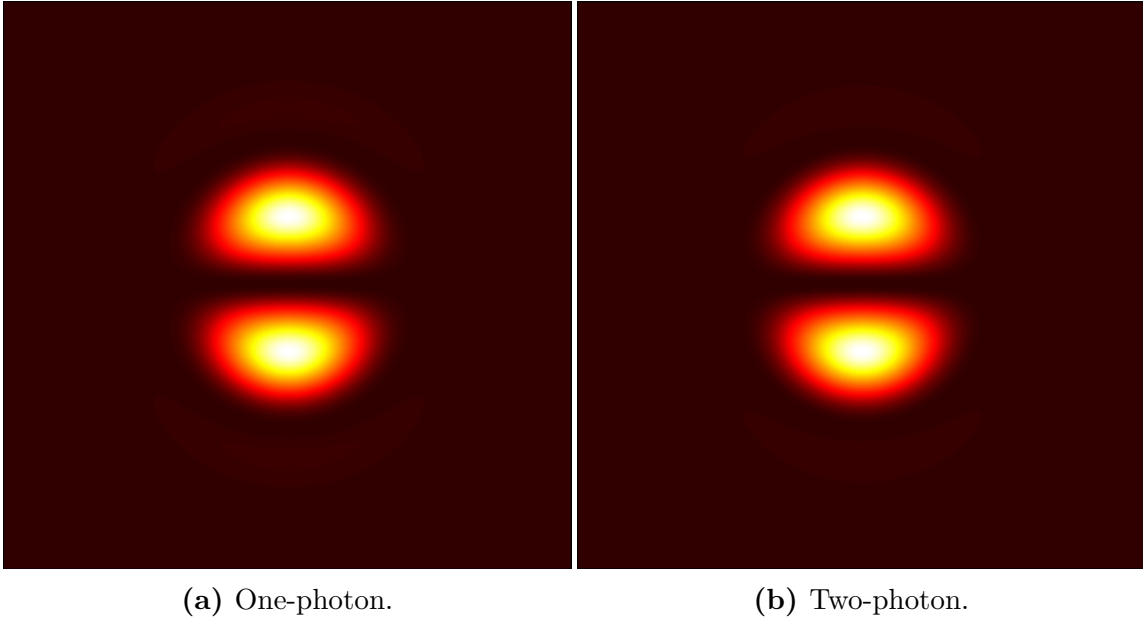


Figure 3.17: Ionization for the resonance with $\varepsilon = -0.96541$ at 950 V/cm.

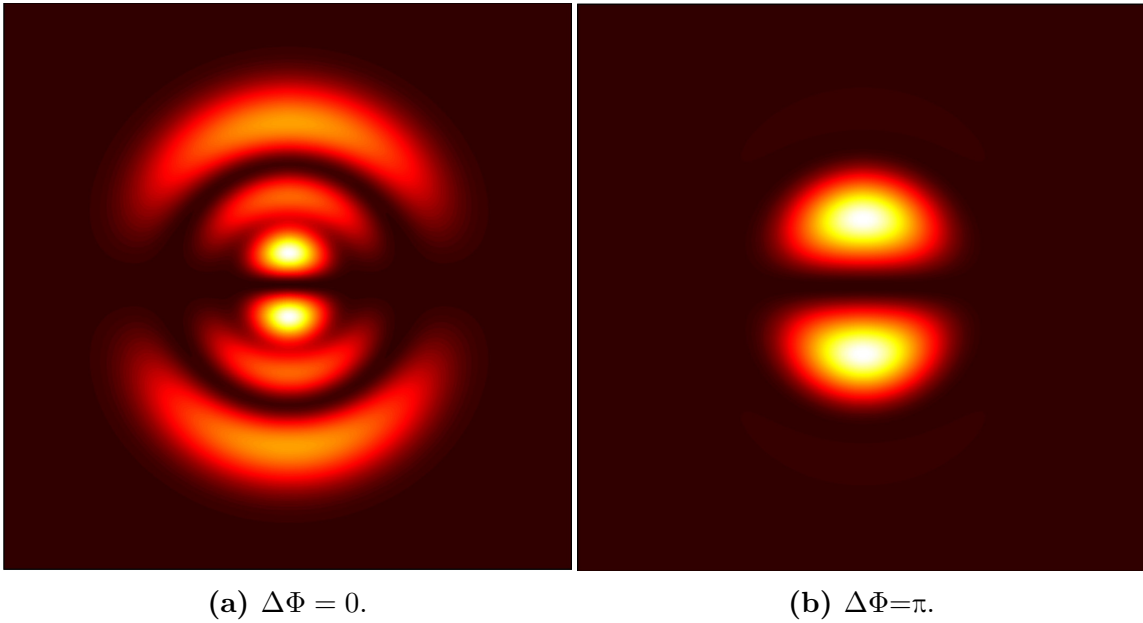


Figure 3.18: Control at $\chi = 3.56$ a.u. for the resonance with $\varepsilon = -0.96541$ at 950 V/cm.

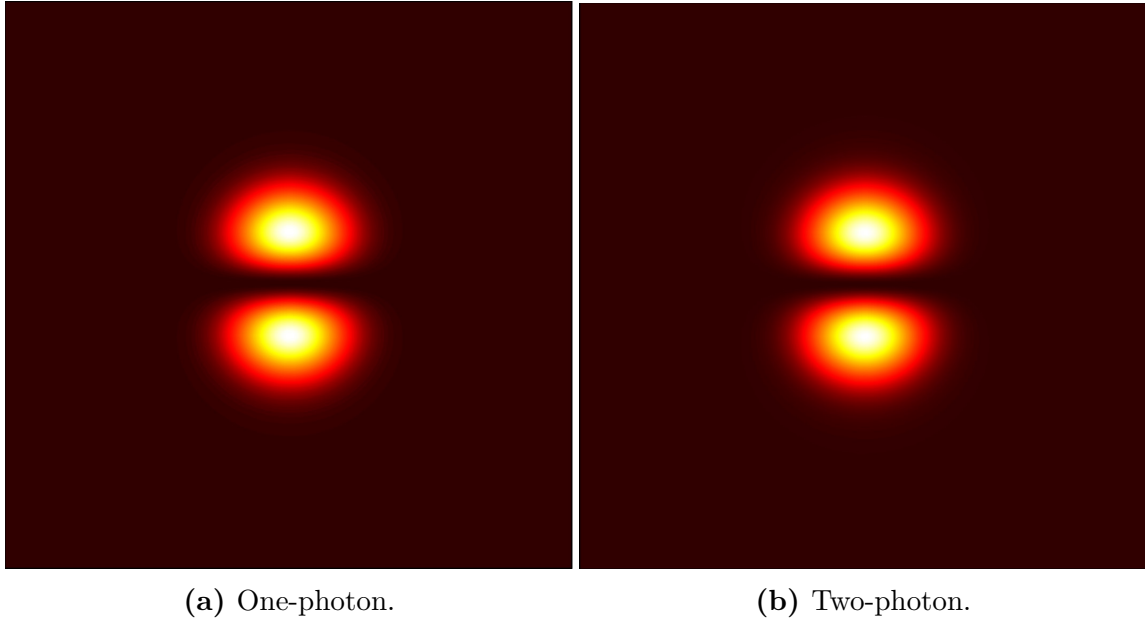


Figure 3.19: Ionization for the resonance with $\varepsilon = -0.96429$ at 950 V/cm.

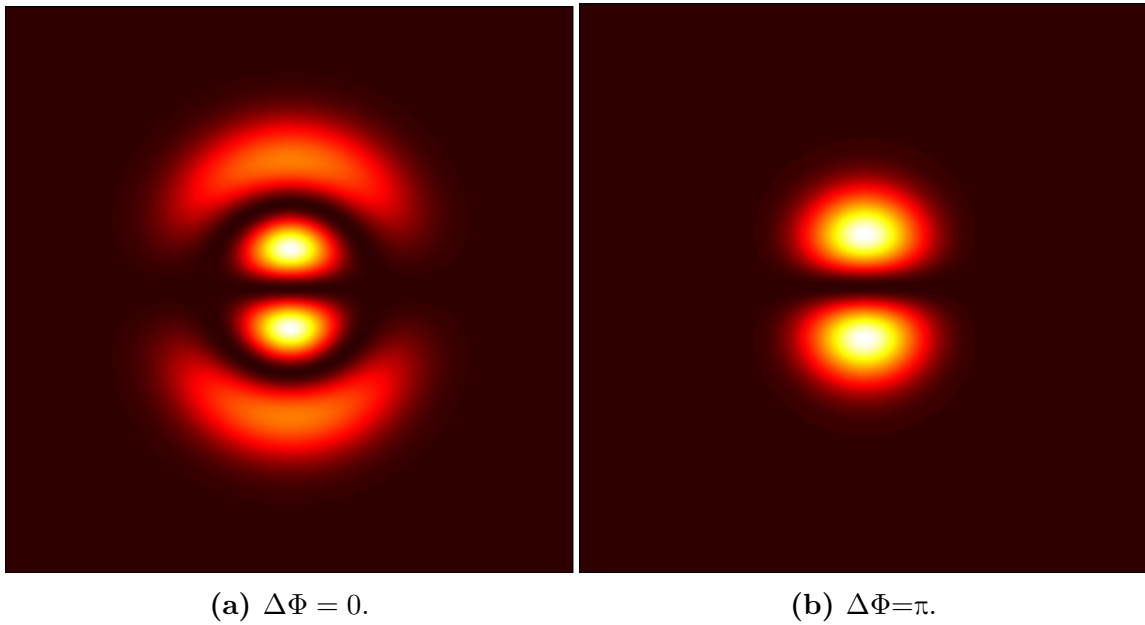


Figure 3.20: Control at $\chi = 7.16$ a.u. for the resonance with $\varepsilon = -0.96429$ at 950 V/cm.

For the $\varepsilon = -0.96073$, the resonant features could be distinctly identified using either single- or two-photon transitions independently, as well as in the $\omega/2\omega$ configuration with $\Delta\Phi = \pi$. This behavior was not observed for the other energy

values at this field. However, as shown in Figure 3.22, the $\omega/2\omega$ with $\Delta\Phi = 0$ the resonance of interest appears more intense.

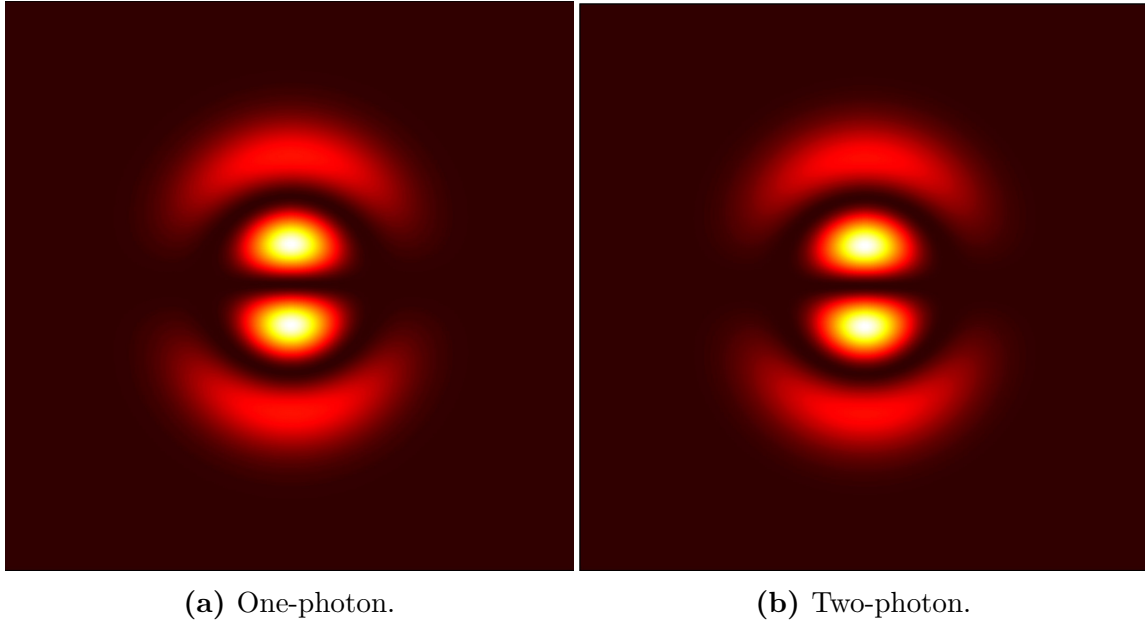


Figure 3.21: Ionization for the resonance with $\varepsilon = -0.96073$ at 950 V/cm.

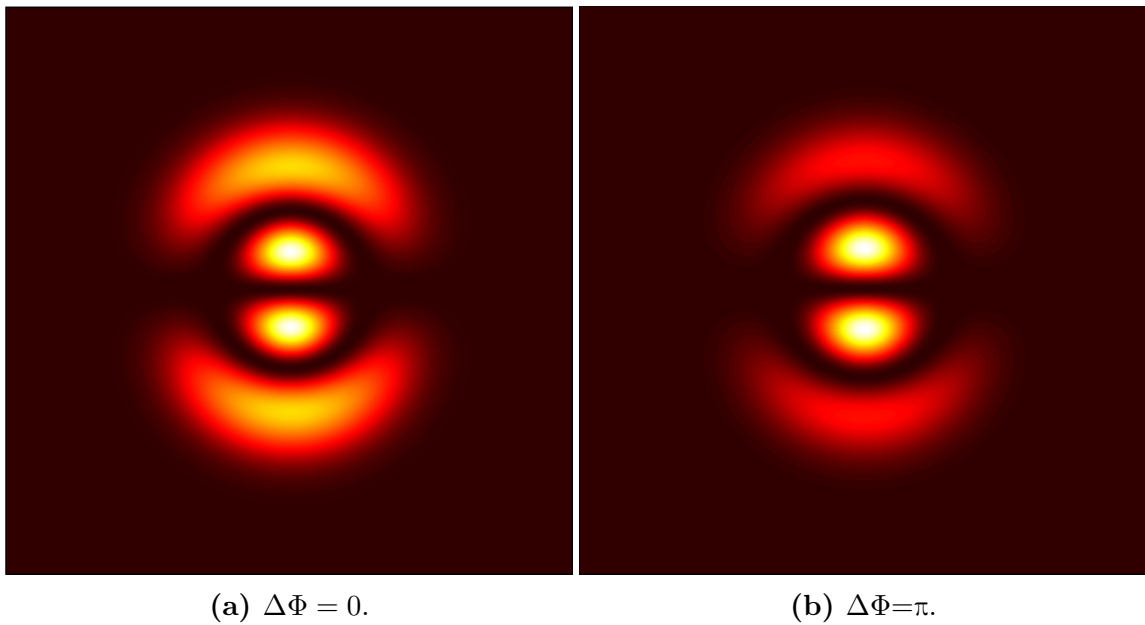


Figure 3.22: Control at $\chi = 7.46$ a.u. for the resonance with $\varepsilon = -0.96073$ at 950 V/cm.

These evaluations clearly demonstrate that by employing the PSCC scheme with

an appropriate selection of energy, field strength, laser intensities, and the phase difference between the two fields, it is possible to selectively extract the resonant features of a specific target state while minimizing the contribution from the continuum.

3.2 PSCC with many continuum channels

An intriguing feature of slow photoelectron imaging is the appearance of two distinct concentric patterns in the recorded images [45, 46]. The outer structure is related to electron trajectories that follow a classical description from the source to the detector. These trajectories are intricate and cross the negative z axis at least once during their route, this contribution is called indirect. The inner structure, known as the direct contribution, emerges only for $E \geq E_{dir} \approx 0.775E_{sp}$, which translates to $\varepsilon_{dir} = -0.775$, and originates from simple quasi-parabolic trajectories that do not meet the z axis. These contributions are categorized based on the electron's launch angle β relative to the electric field (with $\beta = 0$ denoting the ejection along the field direction $+z$ while $\beta = \pi$ denotes the ejection opposite to the field direction $-z$ and towards the PSD plane). For all escaping trajectories, the launch angles satisfies $\beta \geq \beta_c \equiv 2 \arcsin [E/E_{sp}] (E \leq 0)$, whereas for $\beta \leq \beta_c$ the electron remains classically bound. Direct trajectories are differentiated from indirect ones by the angle β_0 , where the corresponding trajectory intersects the z axis at infinity. Indirect trajectories are associated with launch angles within the range $[\beta_c, \beta_0]$, while direct ones correspond to angles in $[\beta_0, \pi]$ [12, 47].

For both excitation schemes, our calculations concentrate on two specific, near ε_{dir} energy values, $\varepsilon = -0.78$ and $\varepsilon = -0.7$, to investigate the contributions from both direct and indirect trajectories.

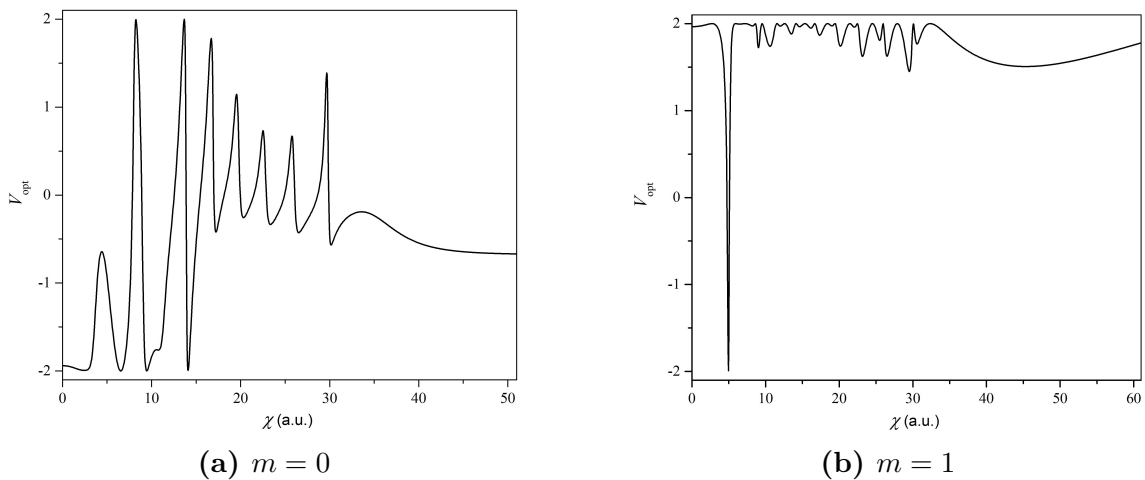


Figure 3.23: Optimum contrast V_{opt} as a function of χ for $\varepsilon = -0.7$ and field strength 1 kV/cm.

For the fields analyzed in the previous section, we examined the contributions from both direct and indirect trajectories. Specifically, for the $m = 0$ scenario at 940 V/cm, V_{opt} as a function of χ is shown in Figure 3.24 and 3.25 for $\varepsilon = -0.78$ and $\varepsilon = -0.7$, respectively. At these energies, numerous open continuum channels are available: specifically, for $\varepsilon = -0.78$, channels range from $n_1 = 0$ to $n_1 = 9$, while for $\varepsilon = -0.7$, channels extend from $n_1 = 0$ to $n_1 = 13$.

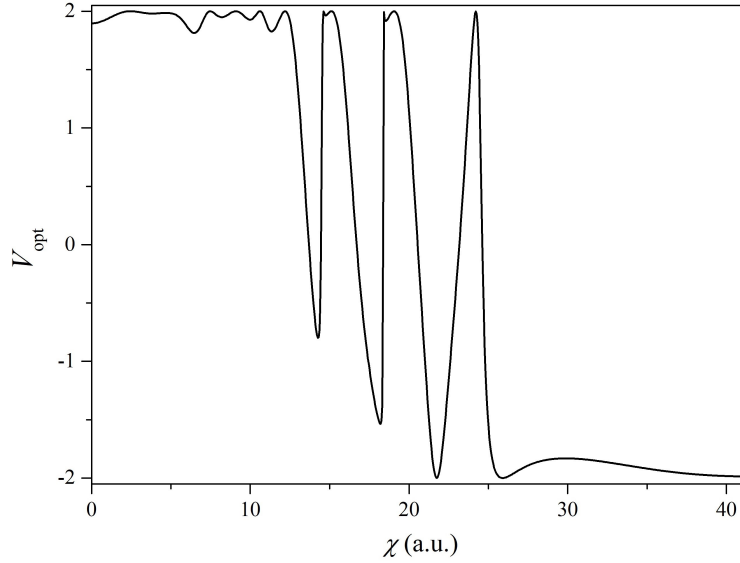


Figure 3.24: $V_{opt}(\chi)$ for the $m = 0$ scenario, $\varepsilon = -0.78$, and field strength 940 V/cm

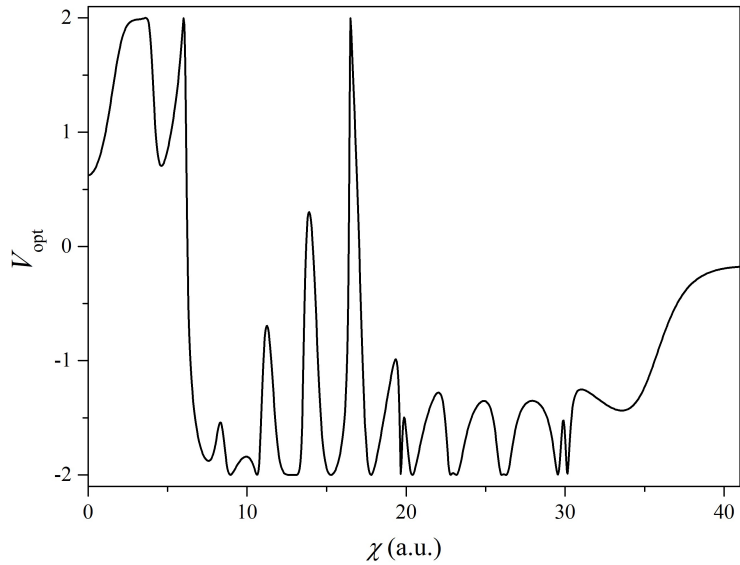


Figure 3.25: $V_{opt}(\chi)$ for the $m = 0$ scenario, $\varepsilon = -0.7$, and field strength 940 V/cm

The results indicate that control over the entire image is not feasible, due to the sign changes exhibited by $V_{opt}(\chi)$ across the entire χ radius. However, as it can be seen from Figure 3.24, for $\varepsilon = -0.78$, control may still be possible for small values of $\chi \leq 5$, where it remains relatively stable. In contrast, for $\varepsilon = -0.7$, such control is not achievable, as $V_{opt}(\chi)$ shows sign changes across the entire χ range.

The corresponding evaluation for the $m = 1$ scenario is presented in Figures 3.26 and 3.27 at 935 V/cm. In this case, the open continuum channels range from $n_1 = 0$ to $n_1 = 9$ for $\varepsilon = -0.78$, while for $\varepsilon = -0.7$, they extend from $n_1 = 0$ to $n_1 = 12$.

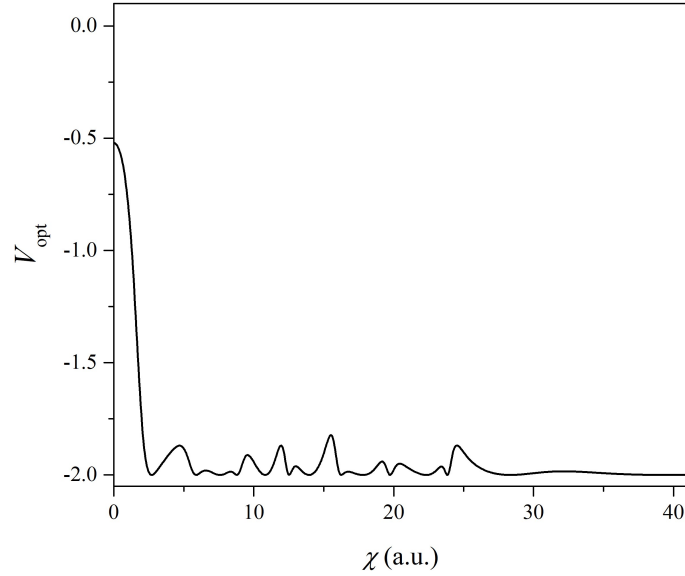


Figure 3.26: V_{opt} $m = 1$ $F=935$ $\varepsilon = -0.78$

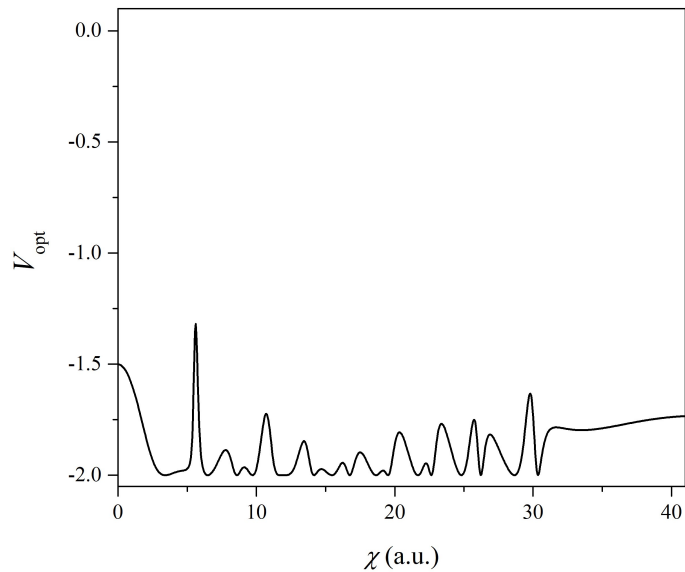


Figure 3.27: V_{opt} $m = 1$ $F=935$ $\varepsilon = -0.7$

The results for V_{opt} , in the $|m| = 1$ scenario, did not demonstrate any sign changes, suggesting the possibility to achieve control in certain χ ranges. Nonetheless, the values of V_{opt} were not relatively constant, indicating that manipulation of the image remains challenging.

Consequently, as we explored higher energy regions deeper within the continuum the number of coupling channels increases significantly. An important consequence is that $V_{opt}(\chi)$ begins to exhibit sign changes, as depicted in the previous figures. This shift introduces significant difficulties in achieving control across the entire image, as the interference patterns become more complex.

Conclusions

This work presents the theoretical investigation of a scheme of simultaneous one- and two-photon excitation of the Stark states using two coherent laser beams with frequencies 2ω and ω , respectively, and an experimentally controlled phase difference $\Delta\Phi$ between them. This phase-sensitive coherent excitation approach was designed to effectively record and accentuate resonant features on the photoionization microscopy images. As opposed to earlier studies dealing with the application of coherent control in the photoionization microscopy of hydrogen atoms [30], here we have applied the Harmin-Fano Stark theory to a non-hydrogenic atom, specifically sodium (Na) atom, in order to address the mixing of resonant and continuum channels characteristic of these atoms. Moreover, we have considered two excitation schemes, one with the $3s$ ground state as the initial state (leading to $m = 0$ final Stark states), and the other where the initial state is the $3p$ first excited one (leading to $|m| = 1$ final Stark states). The latter exhibits certain important advantages from an experimental point of view and in conjunction with the VMI spectrometers/microscopes employed for these studies so far.

The choice of an Alkali metal atom, is guided by the fact that the employed frame transformation theory, as formulated by Harmin, is better adapted for the study of the Stark effect of these atoms. Furthermore, Na atom ($Z = 11$) is selected among the Alkalies because it is almost isoelectronic to Mg ($Z = 12$) which has been studied experimentally [19] and where the resonance features in the recorded images were quite difficult to observe without applying any phase-sensitive coherent excitation scheme. In fact, our calculations have shown that photoionization microscopy images corresponding to solely single- or solely two-photon excitation of Na, rarely show any resonant features. This is, however, indeed achieved when the phase-sensitive bichromatic excitation is employed. Of course, this accomplishment requires careful selection of all the relevant parameters. Particularly, the selected energy range needs to lie just above the saddle point energy where the number of continua is small (since it is proved that a large number of them is detrimental). Second, the $|m| = 1$ results are far more promising than the $m = 0$ ones. This fact can not as of yet be generalized, but the greater difficulty with which resonant features can be uncovered in this case may be attributed to the highly core-penetrating $m = 0$ states. Finally, since the phase sensitive coherent control over the images exhibits a generally strong dependence on the image radius ρ (or χ), control optimization at

specific ρ values that bring out the resonant features is absolutely necessary. Thus, uniform optimization across a given resonant image is fairly complex.

To further enhance our understanding on the proposed theoretical method, several actions and improvements can be considered. First, the conditions under which the resonant features are more evident need to be examined in more detail and in conjunction with the n_1 -channel admixture coefficients, and particularly with the evolution of these coefficients across the Stark-level avoided crossings. Second, the electron spin and fine structure effects can be included for expanding the presently proposed method to even heavier Alkali atoms. To this end the refinements of Harmin-Fano Stark theory proposed in [36, 48] could be incorporated, improving the computational accuracy. This, in turn, could guide the design of near-future experimental campaigns and the development of more precise photoionization microscopy techniques in atomic, as well as in molecular systems.

In conclusion, the proposed theoretical framework for the phase sensitive coherent control scheme offers a promising approach investigating resonant behaviors in photoionization microscopy of non-hydrogenic atoms and lays the groundwork for more accurate, experimentally verifiable studies in multi-photon excitation under the presence of an electric field.

Appendix A

Alkali atoms: Energy levels and Wave functions

To calculate the required wave functions and energy levels of a specific atom, it is essential to solve the corresponding Schrödinger equation. In many occasions, the focus is on the wave functions and (ground as well as excited) energy levels of a valence electron interacting with the residual ionic core. In such cases, the interaction can be adequately modeled with a valence electron in an effective potential. For the free (i.e. without any external perturbations) Alkali atoms, a single valence electron outside closed (sub)shells, this potential is spherically symmetric and the Schrödinger equation writes,

$$\left[-\frac{1}{2}\nabla^2 + U(\mathbf{a}_\ell; r) - E \right] \psi(\mathbf{r}) = 0. \quad (\text{A.1})$$

In Eq.(A.1), the spherically symmetric potential $U(\mathbf{a}_\ell; r)$ is atom-specific and depends on the parameter set \mathbf{a}_ℓ that, in turn, depends on the angular momentum quantum number ℓ of the valence electron. This potential is subject to key constraints at specific limits. Near the nucleus, $r \rightarrow 0$, the potential must asymptotically approach $-Z/r$, reflecting the full nuclear charge. At large distances, $r \rightarrow \infty$, it transitions to $-Z_{eff}/r$, where Z_{eff} denotes the effective charge experienced by the valence electron, accounting for the screening effects of inner-shell electrons. Furthermore, when multi-photon transitions are of interest, one needs to perturbatively compute the relevant virtual states. The virtual state wavefunctions are determined by solving the Dalgarno-Lewis equation, which, for the aforementioned Alkali atoms, is expressed as,

$$\left[-\frac{1}{2}\nabla^2 + U(\mathbf{a}_\ell; r) - E_\nu \right] \psi_\nu = -\hat{T}\psi_i. \quad (\text{A.2})$$

where $E_\nu = (E + E_i)/2$ is the virtual state energy, $U(\mathbf{a}_\ell; r)$ is the same parametric potential used in Eq.(A.1) and \hat{T} is a transition operator. In the present work, the required parametric potential is obtained from the literature [28] and has the form,

$$U(\mathbf{a}_\ell; r) = -\frac{1}{r} \left[Z_{eff} + (Z - 1)e^{a_1 r} - r(a_3 + a_4 r)e^{a_2 r} \right] - \frac{a_c}{2r^4} f_c(r_c^\ell; r) \quad (\text{A.3})$$

where a_c is the static dipole polarizability of the positive-ion core and $f_c(r_c^\ell; r)$ is a cut-off function dealing with the inappropriate behavior of the $-a_c/2r^4$ term at short distances ($r \rightarrow 0$). The optimized parameters, a_i , $i = 1, 2, 3, 4$ and a_c , are listed in Table A.1 as they were presented in [28]. The cut-off function originally proposed in [49] and subsequently utilized in [28] was found to be numerical unstable. As a result, an alternative function was adopted to achieve the desired stability and level of precision, expressed in the following form,

$$f_c(r_c^\ell; r) = \frac{r^6}{\sqrt{r^{12} + (r_c^\ell)^{12}}}. \quad (\text{A.4})$$

The cut-off radii values r_c^ℓ were adjusted to match the experimental energy levels for each specific Alkali metal atom of interest, within the range $25 \leq n \leq 45$. However, the remaining parameters in the parametric potential, as outlined in [28], were preserved without modification. The results for the cut-off radii for the Alkali atom employed in the present work are summarized in Table A.2.

Table A.1: Static dipole polarizability a_c and alpha parameters for the ℓ -dependent model potential $U(\mathbf{a}_\ell; r)$ for the sodium (Na) atom, as taken from [28].

Alkali Atom	Na (Z=11)
a_c	0.9448
$\ell = 0$	
a_1	4.82223117
a_2	2.45449865
a_3	-1.12255048
a_4	-1.42631393
$\ell = 1$	
a_1	5.08382502
a_2	2.18226881
a_3	-1.19534623
a_4	-1.03142861
$\ell = 2$	
a_1	3.53324124
a_2	2.48697936
a_3	-0.75688448
a_4	-1.27852357
$\ell \geq 3$	
a_1	1.11056646
a_2	1.05458759
a_3	1.73203428
a_4	-0.09265696

Table A.2: Presently evaluated cut-off radii r_c^ℓ for Na atom. For $r_c^{\ell \geq 3}$ the value is directly taken from [28].

Alkali Atom	$r_c^{\ell=0}$	$r_c^{\ell=1}$	$r_c^{\ell=2}$	$r_c^{\ell \geq 3}$
Na	0.46489422	0.46662	0.61455312	28.6735059

Our calculations provided all the wave functions and energy levels of interest here. Particular attention was paid to the determination of the near-threshold Rydberg series quantum defects that enter as inputs to the Harmin-Fano Frame Transformation Stark effect Theory. These near-threshold quantum defects are listed in Table A.3. However, Harmin-Fano Stark theory requires that quantum defects to be transformed as [34],

$$\tilde{\mu}_\ell \rightarrow \left(\mu_\ell + \frac{1}{2} \right) (\text{mod} 1) - \frac{1}{2}. \quad (\text{A.5})$$

in order to be confined within the $-1/2 < \tilde{\mu}_\ell < 1/2$ branch. The transformed quantum defects for Na are given in Table A.4.

Table A.3: Quantum Defects of Na.

Alkali Atom	$\mu_{\ell=0}$	$\mu_{\ell=1}$	$\mu_{\ell=2}$	$\mu_{\ell=3}$
Na	1.34796	0.855	0.01554	0.00145

Table A.4: Quantum Defects of Na based on Harmin's transformation.

Alkali Atom	$\tilde{\mu}_{\ell=0}$	$\tilde{\mu}_{\ell=1}$	$\tilde{\mu}_{\ell=2}$	$\tilde{\mu}_{\ell=3}$
Na	0.34796	-0.145	0.01554	0.00145

Let us now describe the evaluation of the transition matrix elements from an initial ψ_i to a final $\psi_{\ell,m}$ state, both expressed in spherical coordinates,

$$D_\ell^m = \langle \psi_{\ell,m} | \hat{T} | \psi_i \rangle \quad (\text{A.6})$$

where $\hat{T} = \boldsymbol{\epsilon} \cdot \mathbf{r}$. Using linearly polarized laser fields, with polarization vectors parallel to the static electric field along the z -direction (π -polarization), the transition operator is expressed as,

$$\hat{T} = z = r \cos \theta = r \sqrt{\frac{4\pi}{3}} Y_1^0 \quad (\text{A.7})$$

with Y_ℓ^m a spherical harmonic function. Furthermore, the form of the parametric potential in Eq.(A.3) leads to a change in the radial part of the operator \hat{T} , which is given as [49–51],

$$r \rightarrow r_{eff} = r \left[1 - \frac{a_d(\omega)}{r^3} \sqrt{f_c(\bar{r}_c; r)} \right]. \quad (\text{A.8})$$

Here $a_d(\omega)$ represents the dynamic dipole polarizability of the atom evaluated at the transition frequency ω . In our case, $a_d(\omega)$ can be set equal to the static dipole polarizability a_c , as proposed in [49–51]. The form of the cut-off function follows the same structure as in Eq.(A.4), with the appropriate definition of the cut-off radius, as it was outlined in [49],

$$\bar{r}_c = \sqrt{r_c^{(i)\ell} r_c^{(f)\ell'}} \quad (\text{A.9})$$

where $r_c^{(i)\ell}$, $r_c^{(f)\ell'}$ are the cut-off radii of the initial and final states, respectively. Regarding the two-photon transitions, though, the cut-off function that was used had the form,

$$\bar{r}_c^\ell = (r_c^{(i)\ell_i} r_c^{(f)\ell_f})^{1/4} (r_c^{(\nu)\ell_\nu})^{1/2}. \quad (\text{A.10})$$

The terms $r_c^{(i)\ell_i}$, $r_c^{(f)\ell_f}$, $r_c^{(\nu)\ell_\nu}$ denote the calculated cut-off radii corresponding to the initial, final and virtual states, respectively. This methodology enabled an accurate evaluation of the virtual state wave functions, ensuring consistency with the chosen model parameters.

The subsequent step involves calculating the zero-field transition matrix elements for the one- and two-photon excitation processes. Then, the parameters $\Lambda^{(2)}$ and $\Lambda^{(1)}$ defined in Section 2.4 are given as,

$$\Lambda^{(2)} \equiv \frac{A_{\ell'm'}^{(2)} R_{\ell'm'}^{(2)}}{A_{\ell m}^{(2)} R_{\ell m}^{(2)}} \quad \Lambda^{(1)} \equiv \frac{A_{\ell m}^{(2)} R_{\ell m}^{(2)}}{A_{\ell m}^{(1)} R_{\ell m}^{(1)}} \quad (\text{A.11})$$

where now the matrix elements of Eq.(A.6) are decomposed into an angular factor and a radial transition matrix element $R_{\ell m}^{(1)}$ and $R_{\ell m}^{(2)}$ for single- and two-photon transitions, respectively. The latter are given by,

$$R_{\ell,m}^{(2)} = \int P_\nu^{(1)} r_{eff} P_{f,\ell} dr \quad R_{\ell,m}^{(1)} = \int P_i r_{eff} P_f dr. \quad (\text{A.12})$$

The angular factors are defined as,

$$A_{\ell m} = \sqrt{\frac{4\pi}{3}} \int Y_{\ell_i}^{*m_i} Y_1^0 Y_\ell^m d\Omega \quad (\text{A.13})$$

where ℓ , m correspond to the final state, while ℓ_i , m_i refer to the initial state of the transition, which may also denote a virtual state in the case of a two-photon excitation. In the equation above, we utilized the definition of the transition operator from Eq.(A.7). The values of the angular factors are summarized in Table A.5, based on the quantum numbers ℓ and m permitted by the selection rules for each excitation scheme analyzed in Section 2.4.

Table A.5: Angular factors for the transitions analyzed in Section 2.4.

A_{00}	A_{10}	A_{20}	A_{11}	A_{21}	A_{31}
$1/\sqrt{3}$	$1/\sqrt{3}$	$2/\sqrt{15}$	$-1/\sqrt{5}$	$-1/\sqrt{5}$	$-2\sqrt{2/35}$

Finally, for the scheme illustrated in Figure 2.3, the computed values of Eq.(A.11) are $\Lambda^{(2)} = -1.65$ and $\Lambda^{(1)} = -2341.1$, while for the one presented in Figure 2.5, the corresponding values are $\Lambda^{(2)} = -160.1$ and $\Lambda^{(1)} = 1542.9$.

Bibliography

- ¹V. D. Kondratovich and V. N. Ostrovsky, “Resonance and interference phenomena in the photoionisation of a hydrogen atom in a uniform electric field. i. resonances below and above the potential barrier”, *J. Phys. B* **17**, 1981 (1984).
- ²V. D. Kondratovich and V. N. Ostrovsky, “Resonance and interference phenomena in the photoionisation of a hydrogen atom in a uniform electric field. ii. overlapping resonances and interference”, *J. Phys. B* **17**, 2011 (1984).
- ³V. D. Kondratovich and V. N. Ostrovsky, “Resonance and interference phenomena in the photoionisation of a hydrogen atom in a uniform electric field. iii. comparison with recent experimental and theoretical results”, *J. Phys. B* **23**, 21 (1990).
- ⁴V. D. Kondratovich and V. N. Ostrovsky, “Resonance and interference phenomena in the photoionization of a hydrogen atom in a uniform electric field. iv. differential cross sections”, *J. Phys. B* **23**, 3785 (1990).
- ⁵H. Bethe and E. Salpeter, *Quantum mechanics of one- and two-electron atoms* (Springer Berlin Heidelberg, 2013).
- ⁶T. F. Gallagher, *Rydberg atoms* (Cambridge University Press, 1994).
- ⁷C. Blondel, C. Delsart, and F. Dulieu, “The photodetachment microscope”, *Phys. Rev. Lett.* **77**, 3755 (1996).
- ⁸C. Nicole, H. L. Offerhaus, M. J. J. Vrakking, F. Lépine, and C. Bordas, “Photoionization microscopy”, *Phys. Rev. Lett.* **88**, 133001 (2002).
- ⁹C. Bordas, F. Lépine, C. Nicole, and M. J. J. Vrakking, “Semiclassical description of photoionization microscopy”, *Phys. Rev. A* **68**, 012709 (2003).
- ¹⁰F. Lépine, C. Bordas, C. Nicole, and M. J. J. Vrakking, “Atomic photoionization processes under magnification”, *Phys. Rev. A* **70**, 033417 (2004).
- ¹¹S. Cohen, M. M. Harb, A. Ollagnier, F. Robicheaux, M. J. J. Vrakking, T. Barillot, F. Lépine, and C. Bordas, “Wave function microscopy of quasibound atomic states”, *Phys. Rev. Lett.* **110**, 183001 (2013).
- ¹²S. Cohen, M. M. Harb, A. Ollagnier, F. Robicheaux, M. J. J. Vrakking, T. Barillot, F. Lépine, and C. Bordas, “Photoionization microscopy of the lithium atom: wave-function imaging of quasibound and continuum stark states”, *Phys. Rev. A* **94**, 013414 (2016).

- ¹³A. S. Stodolna, F. Lépine, T. Bergeman, F. Robicheaux, A. Gijsbertsen, J. H. Jungmann, C. Bordas, and M. J. J. Vrakking, “Visualizing the coupling between red and blue stark states using photoionization microscopy”, *Phys. Rev. Lett.* **113**, 3002 (2014).
- ¹⁴A. S. Stodolna, A. Rouzée, F. Lépine, S. Cohen, F. Robicheaux, A. Gijsbertsen, J. H. Jungmann, C. Bordas, and M. J. J. Vrakking, “Hydrogen atoms under magnification: direct observation of the nodal structure of stark states”, *Phys. Rev. Lett.* **110**, 213001 (2013).
- ¹⁵L. B. Zhao and J. B. Delos, “Dynamics of electron wave propagation in photoionization microscopy. ii. quantum-mechanical formulation”, *Phys. Rev. A* **81**, 053418 (2010).
- ¹⁶L. B. Zhao, D. H. Xiao, and I. I. Fabrikant, “Simulation of wave-function microscopy images of stark resonances”, *Phys. Rev. A* **91**, 043405 (2015).
- ¹⁷P. Kalaitzis, S. Danakas, F. Lépine, C. Bordas, and S. Cohen, “Photoionization microscopy: hydrogenic theory in semiparabolic coordinates and comparison with experimental results”, *Phys. Rev. A* **97**, 053412 (2018).
- ¹⁸M. L. Zimmerman, M. G. Littman, M. M. Kash, and D. Kleppner, “Stark structure of the rydberg states of alkali-metal atoms”, *Phys. Rev. A* **20**, 2251 (1979).
- ¹⁹P. Kalaitzis, S. Danakas, C. Bordas, and S. Cohen, “Near-saddle-point-energy photoionization microscopy images of stark states of the magnesium atom”, *Phys. Rev. A* **99**, 023428 (2019).
- ²⁰P. Giannakeas, F. Robicheaux, and C. H. Greene, “Photoionization microscopy in terms of local-frame-transformation theory”, *Phys. Rev. A* **91**, 043424 (2015).
- ²¹F. Texier, “Runge-lenz wave packet in multichannel stark photoionization”, *Phys. Rev. A* **71**, 013403 (2005).
- ²²L. B. Zhao, “Disappearing resonance tunneling in photoelectron emission”, *Europhysics Letters* **109**, 23002 (2015).
- ²³L. B. Zhao, I. I. Fabrikant, M. L. Du, and C. Bordas, “Test of the stark-effect theory using photoionization microscopy”, *Phys. Rev. A* **86**, 053413 (2012).
- ²⁴M. Shapiro, J. W. Hepburn, and P. Brumer, “Simplified laser control of unimolecular reactions: simultaneous (ω_1, ω_3) excitation”, *Chem. Phys. Lett.* **149**, 451 (1988).
- ²⁵M. Shapiro and P. Brumer, *Coherent control of atomic, molecular, and electronic processes*, Vol. 42, Ad. At. Mol. Opt. Phys. (Academic Press, 2000), p. 287.
- ²⁶C. Chen, Y.-Y. Yin, and D. S. Elliott, “Interference between optical transitions”, *Phys. Rev. Lett.* **64**, 507 (1990).
- ²⁷H. G. Muller, P. H. Bucksbaum, D. W. Schumacher, and A. Zavriyev, “Above-threshold ionisation with a two-colour laser field”, *J.Phys. B* **23**, 2761 (1990).
- ²⁸M. Marinescu, H. R. Sadeghpour, and A. Dalgarno, “Dispersion coefficients for alkali-metal dimers”, *Phys. Rev. A* **49**, 982 (1994).

- ²⁹R. J. Damburg and V. V. Kolosov, “A hydrogen atom in a uniform electric field”, *J. Phys. B* **9**, 3149 (1976).
- ³⁰P. Kalaitzis, D. Spasopoulos, and S. Cohen, “One- and two-photon phase-sensitive coherent-control scheme applied to photoionization microscopy of the hydrogen atom”, *Phys. Rev. A* **100**, 043409 (2019).
- ³¹K. Ferentinou, S. Danakas, C. Bordas, and S. Cohen, “Glory interference spectroscopy in sr atom”, *Journal of Physics B: Atomic, Molecular and Optical Physics* **57**, 115002 (2024).
- ³²L. Landau and E. Lifshitz, *Quantum mechanics: non-relativistic theory*, Vol. 3 (Elsevier, 2013).
- ³³D. A. Harmin, “Theory of the nonhydrogenic stark effect”, *Phys. Rev. Lett.* **49**, 128 (1982).
- ³⁴D. A. Harmin, “Theory of the stark effect”, *Phys. Rev. A* **26**, 2656 (1982).
- ³⁵U. Fano, “Stark effect of nonhydrogenic rydberg spectra”, *Phys. Rev. A* **24**, 619 (1981).
- ³⁶P. Giannakeas, C. H. Greene, and F. Robicheaux, “Generalized local-frame- transformation theory for excited species in external fields”, *Phys. Rev. A* **94**, 013419 (2016).
- ³⁷D. A. Harmin, “Hydrogenic stark effect: properties of the wave functions”, *Phys. Rev. A* **24**, 2491 (1981).
- ³⁸D. A. Harmin, “Analytical study of quasidiscrete stark levels in rydberg atoms”, *Phys. Rev. A* **30**, 2413 (1984).
- ³⁹A. Dalgarno, J. T. Lewis, and D. R. Bates, “The exact calculation of long-range forces between atoms by perturbation theory”, *Proc. R. Soc. London. Ser. A.* **233**, 70 (1955).
- ⁴⁰V. Astapenko, “Coherent phase control of excitation of atoms by bichromatic laser radiation in an electric field”, *Quantum Electronics* **35**, 541 (2005).
- ⁴¹S. Cohen, “Phase sensitive coherent control of atomic excitation in the presence of static electric fields: a frame transformation stark theory approach”, *J. Phys. B* **44**, 205402 (2011).
- ⁴²M. M. Harb, S. Cohen, E. Papalazarou, F. Lépine, and C. Bordas, “Transfer-matrix-based method for an analytical description of velocity-map-imaging spectrometers”, *Rev. Sc. I.* **81**, 125111 (2010).
- ⁴³A. Bolovinos, S. Cohen, and I. Lontos, “One- and two-photon phase-sensitive coherent control of total ionization yields in the presence of static electric fields”, *Phys. Rev. A* **77**, 023413 (2008).
- ⁴⁴J. Peatross and M. Ware, *Physics of light and optics* (2015).

- ⁴⁵C. Nicole, I. Sluimer, F. Rosca-Pruna, M. Warntjes, M. Vrakking, C. Bordas, F. Texier, and F. Robicheaux, “Slow photoelectron imaging”, *Phys. Rev. Lett.* **85**, 4024–4027 (2000).
- ⁴⁶C. Nicole, H. L. Offerhaus, M. J. J. Vrakking, F. Lépine, and C. Bordas, “Photoionization microscopy”, *Phys. Rev. Lett.* **88**, 133001 (2002).
- ⁴⁷P. Kalaitzis, S. Danakas, K. Ferentinou, F. Lépine, C. Bordas, and S. Cohen, “Glory oscillations in photoionization microscopy: connection with electron dynamics and stark spectral structures in the continuum”, *Phys. Rev. A* **102**, 033101 (2020).
- ⁴⁸V. G. Ushakov, V. I. Osherov, and E. S. Medvedev, “Analytical s-matrix derivation in the theory of the nonhydrogenic stark effect”, *J. Phys. A* **52**, 385302 (2019).
- ⁴⁹D. W. Norcross, “Photoabsorption by cesium”, *Phys. Rev. A* **7**, 606 (1973).
- ⁵⁰S. Hameed, “Core polarization corrections to oscillator strengths and singlet-triplet splittings in alkaline earth atoms”, *J. Phys. B* **5**, 746 (1972).
- ⁵¹C. E. Theodosiou and S. R. Federman, “Accurate Calculation of Mg II 3s-np Oscillator Strengths”, *The Astrophysical Journal* **527**, 470 (1999).